IEEE Access
Multidisciplinary : Rapid Review : Open Access Journal

Received 14 November 2023, accepted 22 November 2023, date of publication 30 November 2023, date of current version 6 December 2023.

Digital Object Identifier 10.1109/ACCESS.2023.3337872

RESEARCH ARTICLE

Development and High-Fidelity Simulation of Trajectory Tracking Control Schemes of a UUV for Fish Net-Pen Visual Inspection in Offshore Aquaculture

THEIN THAN TUN[1], (Graduate Student Member, IEEE), LOULIN HUANG[1], (Member, IEEE), AND MARK ANTHONY PREECE[2]
[1]School of Engineering, Computer and Mathematical Sciences, Auckland University of Technology, Auckland 1010, New Zealand
[2]New Zealand King Salmon Company, Nelson 7011, New Zealand

Corresponding author: Loulin Huang (loulin.huang@aut.ac.nz)

This work was supported in part by the Blue Economy Cooperative Research Centre (CRC), established and supported under the Australian Government's CRC Program, under Grant CRC-20180101; and in part by the Auckland University of Technology (AUT) through the AUT Doctoral Scholarship.

ABSTRACT Offshore aquaculture fish farming faces labor shortage, safety, productivity and high operating cost issues. Unmanned underwater vehicles (UUVs) are being deployed to mitigate these issues. One of their applications is the fish net-pen visual inspection. This paper aims to develop and simulate with high-fidelity several trajectory tracking control schemes for a UUV to visually inspect a fish net-pen in a standard task scenario in offshore aquaculture under 0.0 m/s, 0.5 m/s and 0.9 m/s underwater current disturbances. Three controllers, namely 1) Proportional-Derivative control with restoring force & moment compensation (Compensated-PD), 2) Proportional-Integral-Derivative control with restoring force & moment compensation (Compensated-PID), and 3) computed torque (or) inverse dynamics control (CTC/IDC) were conducted on a 6 degrees-of-freedom (DoF) BlueROV2 Heavy Configuration dealing with 12 error states (pose and twist). A standard task scenario for the controllers was formulated based on the Blue Endeavour project of the New Zealand King Salmon company located 5 kilometres due north of Cape Lambert, in northern Marlborough. This simulated experimental study gathered and applied many available and physically quantifiable parameters of the fish farm and a UUV called BlueROV2 Heavy Configuration. Results show that while utilizing the minimum thrust, CTC/IDC outperforms Compensated-PID and Compensated-PD in overall trajectory tracking under different underwater current disturbances. Numerical results measured with root-mean-square-error (RMSE), mean-absolute-error (MAE) and root-sum-squared (RSS) are reported for comparison, and simulation results in the form of histograms, bar charts, plots, and video recordings are provided. Future work will explore into advanced controllers, with a specific emphasis on energy-optimal control schemes, accompanied by comprehensive stability and robustness analyses applied to linear and nonlinear UUV models.

INDEX TERMS Trajectory tracking control, compensated-PD, compensated-PID, CTC/IDC, underwater current disturbance, offshore aquaculture, fish net-pen visual inspection, robot operating system (ROS), gazebo physics engine.

I. INTRODUCTION

Aquaculture attracts protein-source food production for the growing population. In Southeast Asia and Asia with the majority of the global population, inland water-based aquaculture has been reported to have existed since the end of the 20th century and for thousands of years in China and spread to the rest of the world [1], [2]. However, aquaculture in inland and nearshore or coastal areas faces constraints of limited land space, farm expansion, environmental impact

The associate editor coordinating the review of this manuscript and approving it for publication was Xiaogang Jin.

on the local ecosystem and conflicting coastal users [3]. Therefore, offshore aquaculture or open ocean farming was introduced as a sustainable way of producing protein source to match the ever-increasing demand. Moreover, it provides natural water exposure to the fish with a cooler temperature. On the other hand, temperature instability & abnormality, coastal warming and climate change have to be considered based on the local oceanographic conditions and the type of breeding species [4]. For instance, due to warm water from coral sea, a recent event of losing up to 42% of mortality of biomass in sea farms was reported by the New Zealand King Salmon Company, the world's largest producer of farmed King (also known as Chinook) salmon and highlighted the role of offshore aquaculture or open ocean farming to minimize such events [5].

Along with its benefits, offshore aquaculture also has its own challenges in deploying manpower offshore, ensuring the safety of the workforce and the site infrastructure and high operating costs. Among the operational requirements of offshore aquaculture, one routine-based mundane but operationally challenging process for an operator is the fish net-pen visual inspection. It covers the inspection of fish net-pen shape, netting, mooring system and biofouling, and it could be extended for a thorough inspection due to the incidents & environmental conditions(e.g., storm and icing) and specific operation (e.g., harvesting and de-lousing treatment). The visual inspection also serves as a part of preventive maintenance to identify biofouling which causes net occlusion, and structural fatigue (e.g., mooring failure and holes) of fish net-pen and reduces water flow resulting in a low oxygen level harmful to the health of fish [6], [7], [8]. Fish net-pen holes were reported to cause the 76% of fish (salmon and rainbow trout) escape [9], [10]. Moreover, the more distant from the shore the aquaculture farm is, the more severe and ferocious the environmental disturbances and conditions are to intensify those factors mentioned above.

Conventionally, a trained diver conducts routine manual visual inspection which is time-consuming and costly. It also requires special equipment & training and implementation of safety protocols and the availability of the offshore workforce. An effective way to handle these challenges is the use of UUVs which can perform fish net-pen inspection tasks with a high degree of autonomy and efficiency [8], [11], [12], [13]. Furthermore, they can be manufactured at a large scale as required for the expansion of the aquaculture industry once standardized and equipped with the required operational tools. Note: The terms Unmanned Underwater Vehicle (UUV), Autonomous Underwater Vehicle (AUV) and Remotely Operated Underwater Vehicle (ROV) are used interchangeably in this paper.

A ROV inspection on fish net-pen using a Doppler Velocity Log (DVL) as a relative localization tool with respect to fish net-pen geometry was reported [8]. The approximation of ROV's pose was used to keep the ROV camera face towards fish net-pen and the line-of-sight (LOS) guidance law was utilized to maneuver the ROV along the circumference of fish net-pen to inspect only in the horizontal plane. Another DVL-based autonomous mission control system on Argus Mini ROV using finite state machine (FSM) to handle inspection-maintenance-repair (IMR) operation in aquaculture was addressed [14]. Results from the simulation framework FhSim and the experimental field tests were reported. UUV localization with a laser vision system (LVS)/ laser camera triangulation for fish net-pen inspection was presented [15], [16]. A vision-based positioning scheme (visual servoing) for fish net-pen inspection using a Blueye Pro ROV was reported with simulation and experimental results [13]. Another vision-based approach using the HippoCampus μAUV, integrated with the Intel RealSense D435i RGB-D camera to adapt the global inspection path to the local path planner which changes according to the shape-shifting nature of fish net-pen was presented [17]. Image processing techniques to detect fish net-pen holes by post-processing the recorded video from a ROV with annotation of spatial and temporal data were proposed [18]. The unconventional use of the omnidirectional surface vehicle (OSV) which has the onboard damage detection algorithm and a mechanism to adjust the depth of the underwater camera to live-stream fish net-pen condition was described [19]. To obtain clear images for fish net-pen inspection, a supervised learning controller in which the current image from BlueROV2 was fed into a convolutional neural network (CNN) to generate a proper trajectory of the ROV was reported [20]. In HEKTOR (Heterogeneous Autonomous Robotic System in Viticulture and Mariculture), a collective intelligence from a light autonomous aerial robot (LAAR), a ROV and an autonomous surface vehicle (ASV) to perform fish net-pen inspection was proposed [21].

The literature mentioned above focuses on the issues of localization, and image processing techniques to identify holes and defects in fish net-pen. Some commonly found control strategies for UUV are proportional-integral-derivative (PID) control, sliding mode control (SMC) [22], [23], model predictive control (MPC) [24], [25] and mixed approach of control strategies [26]. Among them, PID controllers are one of the highly applicable controllers for automation and robotics in both academia and industries [27]. Due to the simplicity in design & implementation and less computational load for a small UUV, they are often implemented as the baseline comparison with other controllers or modified as required [28], [29], [30], [31]. For instance, a comparison between the PID controller and the soft actor-critic (SAC)–deep reinforcement learning– based controller was reported [32]. To tackle the UUV's model nonlinearity, parameter uncertainty and external disturbance, a neural-network-based auto-tune PID controller was reported [33], [34]. For better disturbance rejection, a model-free hybrid controller with intelligent-PID and PD feedforward was proposed [35].

Generally, common findings in existing literature can be identified as follows.

- Majority of reported UUVs are in slender body (like a torpedo) whose hydrodynamic properties are optimized/minimized.
- Many UUVs are relatively heavy and thus, less prone to environmental disturbances (e.g., underwater current) due to their large inertia.
- Most UUVs have low maneuverability resulting from lower DoF (e.g. 3,4 or 5 DoF) under control (e.g., controlling pose and yaw angle only).
- Majority of tracking controllers are simulated without consideration of underwater current disturbances.
- Mostly operational environments are unconstrained.

However, production processes including fish net-pen visual inspection by a UUV in offshore aquaculture are conducted close to the infrastructure (e.g., fish net-pen) in a constrained environment (e.g., mooring system and structural complexity of each fish net-pen design) with environmental disturbances (e.g., varying underwater currents, spatial and temporal changes) [36]. Therefore, most existing UUV systems (e.g., slender body AUVs and UUVs with low maneuverability) and simplified tracking scenarios (e.g., pose and yaw only) cannot meet the process's demands well. To address this problem, in this paper, a standard task scenario of an offshore aquaculture fish net-pen visual inspection for which a highly maneuverable 6 degrees-of-freedom (DoF) BlueROV2 Heavy Configuration with eight thrusters performs a trajectory tracking control is set up first [37]. Note: a 5 DoF BlueROV2 version was utilized by others for general purpose, but it is not suitable to conduct simulation studies on the formulated task scenario [38], [39], [40]. After that, three controllers namely, (1) Proportional-Derivative control with restoring force & moment compensation (Compensated-PD), (2) Proportional-Integral-Derivative control with restoring force & moment compensation (Compensated-PID), and (3) computed torque (or) inverse dynamics control (CTC/IDC) are developed to conduct experimental simulation study on the formulated standard task scenario. The first two controllers account for restoring force & moment resulting from the offset between the centers of gravity and buoyancy in addition to the PD and PID controllers [41]. CTC/IDC controller, also known as feedback linearization controller, compensates nonlinearity of the UUV's model and by choosing PID as the feedback control input, the tracking error converges to zero asymptotically [42]. Compensated-PD and Compensated-PID from the existing Robot Operating System (ROS) project called "Unmanned Underwater Vehicle Simulator" are implemented on BlueROV2 Heavy Configuration [43], [44]. CTC/IDC was additionally contributed to compare the tracking performance. The original repository includes ROS packages in which some underwater gazebo scenes, a few types of UUVs, trajectory generators and existing controllers are provided.

In summary, the main contributions of the work reported in this paper can be described as follows:

- High-fidelity simulation studies in which a highly maneuverable UUV with 6 DoF (BlueROV2 Heavy Configuration with eight thrusters) conducts fish net-pen visual inspection with Compensated-PD, Compensated-PID and CTC/IDC, minimizing 12 error states (pose and twist) under 0.0 m/s, 0.5 m/s and 0.9 m/s underwater current disturbances.
- The UUV's 6-DoF dynamics model and 3-D model of the fish farm established from publicly available information and physically quantifiable parameters of a lightweight BlueROV2 Heavy Configuration (square shape UUV) and the fish farm project specifications.
- Formulation of a standard task scenario for the UUV-based fish net-pen visual inspection in a constrained operational environment in a typical offshore fish farm.
- The ROS packages modified and rectified to be compatible with BlueROV2 Heavy Configuration and the actual fish farm specifications (e.g., diameter and depth of the fish net-pen).
- Validation of the performances of the proposed UUV's trajectory tracking schemes with various metrics such as root-mean-square-error (RMSE), mean-absolute-error (MAE) and root-sum-squared (RSS) along with detailed histograms, plots and simulation video recordings.
- Time & cost saving of the actual deployment of UUVs for their performances being pre-validated with high-fidelity simulation.

The remaining part of this paper is structured as follows. The description of the UUV system is covered by Section II. The UUV's dynamic model is described in Section III. The formulation of a visual inspection task scenario based on the New Zealand King Salmon company's fish farm specifications and its constraints on BlueROV2 Heavy Configuration is presented in Section IV. The trajectory tracking control schemes based on Compensated-PD, Compensated-PID and CTC/IDC are presented in Section V, and the experimental simulation study with detailed simulation parameters is presented in Section VI. The simulation results are discussed in Section VII. Finally, the contribution of this paper and future work are summarized and suggested in Section VIII.

II. UUV SYSTEM

Considering the operational requirements of fish net-pen visual inspection, a chosen UUV must possess a high maneuverability to operate close to the fish net-pen and maneuver smoothly to capture stable visual feedback along a desired path in the presence of environmental disturbances. To do so, an open-sourced UUV platform called BlueROV2 Heavy Configuration as shown in FIGURE 1 to achieve 6 DoF was chosen. It spans across 0.575 m (width), 0.4571 m (length) and 0.2539 m (height) and weighs about 11.5 kg in air with ballast [37]. It is equipped with four vertical thrusters and four horizontal thrusters. The maximum rated depth is 100 m

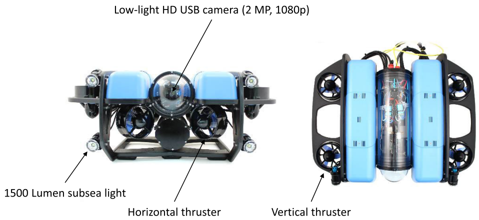

FIGURE 1. BlueROV2 heavy configuration. Front view (left) and Top view (right).

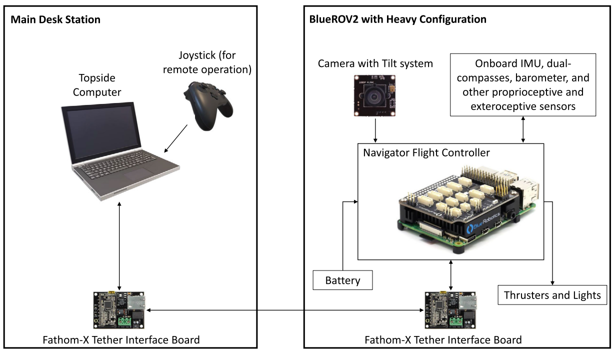

FIGURE 2. System block diagram of BlueROV2 heavy configuration.

with an acrylic electronic enclosure tube and the default BlueROV2 delivers a maximum surge speed of 1.5 m/s. A Blue Robotics 15.6 Ah battery offers a normal use of 2 hours.

As shown in FIGURE 2 for the remote operation, an operator controls BlueROV2 Heavy Configuration using a joystick with the help of the visual feedback from low-light HD USB camera (2 MP, 1080 p). The operator's commands are, via Fathom-X Tether Interface Boards, transmitted to the Navigator Flight Controller which consists of the Navigator board and Raspberry Pi 4. The Navigator board contains multiple modules essential for trajectory tracking control including an onboard inertial measurement unit (IMU), dual compasses, barometer (altitude sensor), pulse-width-modulation (PWM) output channels for the thrusters and analog-to-digital converter (ADC) [45].

For the control experiment in this simulated study, the proposed controllers will execute commands on behalf of the joystick using the ROS localization feedback in Gazebo Physics Engine [46].

III. DYNAMIC MODELLING

To describe the dynamic model of the UUV, the North-East-Down (NED) reference frame and the Society of Naval Architects and Marine Engineers (SNAME) nomenclature as shown respectively in FIGURE 3 and FIGURE 4 are adopted [47], [48].

The x-y plane of North-East-Down (NED) frame $\{n\} : O, \hat{x}, \hat{y}, \hat{z}$ is defined tangential to the surface of the earth, and the x-axis and y-axis point towards the true North and East respectively. There is a coordinate frame attached to the UUV called its body frame $\{b\} : O_b, \hat{x}_b, \hat{y}_b, \hat{z}_b$.

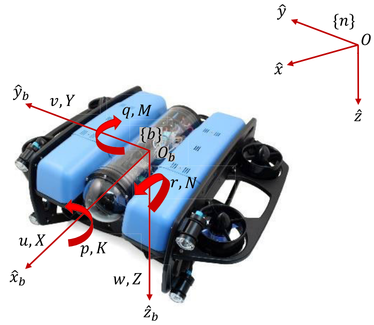

FIGURE 3. BlueROV2 with SNAME nomenclature in NED reference frame.

	Surge	Sway	Heave	Roll	Pitch	Yaw	
Position	x	y	z	ϕ	θ	ψ	Euler Angles
Linear velocities	u	v	w	p	q	r	Angular velocities
Force	X	Y	Z	K	M	N	Moment

FIGURE 4. SNAME nomenclature.

In the SNAME nomenclature, Surge, Sway and Heave denote the terms for translational motions in $\hat{x}_b$, $\hat{y}_b$ and $\hat{z}_b$ respectively, and Roll, Pitch and Yaw denote the terms for rotational motions around $\hat{x}_b$, $\hat{y}_b$ and $\hat{z}_b$ respectively.

A. DYNAMIC MODEL

The 6 DoF nonlinear dynamic model of the UUV system takes account of hydrodynamic forces (added mass and inertia, Coriolis and damping effect), hydrostatic forces (gravitational forces, buoyancy, restoring forces and moments) and underwater current effects as constant disturbance-forces [47].

$$M\dot{\nu} + (C(\nu) + D(\nu))\nu + g(\eta) = \tau(\triangleq Bf_T) + \tau_{current} \quad (1)$$

Indeed, Eqn. (1) is a compact representation of

$$(M_R + M_A)\dot{\nu} + (C_R(\nu) + C_A(\nu) + D_{R_l} + D_{R_q}(\nu))\nu + g(\eta) = \tau(\triangleq Bf_T) + \tau_{current} \quad (2)$$

The definitions of the terms of the dynamic model are listed in TABLE 1. Other miscellaneous terms are listed in TABLE 2 and the expressions of several key matrices in the dynamic model are listed below [47]:

$$M_R = \begin{bmatrix} mI_{3\times3} & -m[r^b_{G/b}\times] \\ m[r^b_{G/b}\times] & I_G - m[r^b_{G/b}\times]^2 \end{bmatrix} = \begin{bmatrix} mI_{3\times3} & 0_{3\times3} \\ 0_{3\times3} & I_G \end{bmatrix} \quad (3)$$

where $r^b_{G/b} = [0 \;\; 0 \;\; 0]^T$ can be defined to simplify M_R. Similarly, the Coriolis-Centripetal acceleration matrix can be

TABLE 1. Description of the dynamic model terms.

Terms	Descriptions
$\eta = [x\ y\ z\ \phi\ \theta\ \psi]^T \in \mathbb{R}^6$	: Pose—position and orientation (Euler angles) vector with respect to (w.r.t) frame $\{n\}$ expressed in frame $\{n\}$
$\nu = [u\ v\ w\ p\ q\ r]^T \in \mathbb{R}^6$	: Twist—linear and angular velocity vector w.r.t frame $\{n\}$ expressed in frame $\{b\}$
$\tau = [X\ Y\ Z\ K\ M\ N]^T \in \mathbb{R}^6$	: Wrench—force and moment vector w.r.t frame $\{b\}$ expressed in frame $\{b\}$
$M \in \mathbb{R}^{6\times6}$	: mass matrix—summation of inertia matrix and added mass matrices
$M_R \in \mathbb{R}^{6\times6}$	: inertia matrix of the rigid body
$M_A \in \mathbb{R}^{6\times6}$	: added mass
$C(\nu) \in \mathbb{R}^{6\times6}$	: Coriolis-Centripetal acceleration matrix
$C_R(\nu) \in \mathbb{R}^{6\times6}$	: Coriolis-Centripetal acceleration matrix of the rigid body
$C_A(\nu) \in \mathbb{R}^{6\times6}$	: Coriolis-Centripetal acceleration matrix of the added mass
$D(\nu) \in \mathbb{R}^{6\times6}$	: damping matrix—summation of linear and quadratic damping matrices
$D_{R_l} \in \mathbb{R}^{6\times6}$	: linear damping matrix
$D_{R_q}(\nu) \in \mathbb{R}^{6\times6}$	: quadratic damping matrix
$g(\eta) \in \mathbb{R}^6$	: gravitational force, buoyancy and the resulting restoring forces and moments
$\tau_{current} \in \mathbb{R}^6$	: constant disturbance contributed by the ocean current
$B \in \mathbb{R}^{6\times8}$	: thruster control/allocation matrix (TCM/TAM)
$f_T \in \mathbb{R}^8$	: input (Thrust) vector

TABLE 2. Description of the miscellaneous terms.

Terms	Descriptions
$[k\times] \in \mathbb{R}^{3\times3}$	: skew-symmetric operation on vector $k \in \mathbb{R}^3$
$diag(k)$	: diagonal matrix with elements of vector $k \in \mathbb{R}^{\mathrm{n}}$
$I_{3\times3}$	: identity matrix
$r^b_{G/b} \in \mathbb{R}^3$	: $[x_G\ y_G\ z_G]^T$: centre of gravity w.r.t frame $\{b\}$ expressed in frame $\{b\}$
$r^b_{B/b} \in \mathbb{R}^3$	: $[x_B\ y_B\ z_B]^T$: centre of buoyancy w.r.t frame $\{b\}$ expressed in frame $\{b\}$
I_G	: moment of inertia expressed in frame $\{b\}$ fixed at the centre of gravity of UUV
$R^n_b(\eta) \in \mathbb{R}^{3\times3}$	: linear velocity transformation from frame $\{b\}$ to frame $\{n\}$
W, B	: gravitational force and buoyancy
$R^n_b(\eta)^{-1} f^n_G \in \mathbb{R}^3$	: $R^n_b(\eta)^{-1}[0\ 0\ W]^T$: gravitational force acting at the centre of gravity of UUV w.r.t frame $\{n\}$ expressed in frame $\{b\}$
$R^n_b(\eta)^{-1} f^n_B \in \mathbb{R}^3$	: -$R^n_b(\eta)^{-1}[0\ 0\ B]^T$: buoyancy force of UUV w.r.t frame $\{n\}$ expressed in frame $\{b\}$

simplied as

$$C_R(\nu) = \begin{bmatrix} m[\nu_2\times] & -m[\nu_2\times][r^b_{G/b}\times] \\ m[r^b_{G/b}\times][\nu_2\times] & -[((I_G - m[r^b_{G/b}\times]^2)\nu_2)\times] \end{bmatrix} = \begin{bmatrix} m[\nu_2\times] & 0_{3\times3} \\ 0_{3\times3} & -[(I_G\nu_2)\times] \end{bmatrix} \tag{4}$$

where $\nu_2 = [p\ q\ r]^T$.

Note: for readability purpose, a vector A with respect to (w.r.t) the inertial (or) NED frame $\{n\}$ expressed in frame $\{b\}$ will be written as A^b instead of $A^b_{/n}$.

The added mass is contributed by the accelerating fluid medium around the accelerating UUV by exerting state-dependent reaction in the opposite direction. In other words, this state-dependent matrix must be accounted for by adding it to the rigid body inertia matrix.

$$\begin{aligned} \tau &: \mathbb{R}^6 \to \mathbb{R}^6 \\ M_A &= \frac{\partial \tau}{\partial \dot{\nu}} \in \mathbb{R}^{6\times6} \end{aligned} \tag{5}$$

Assumption 3.1: During the operation, BlueROV2 Heavy Configuration has three planes of symmetry and was completely submerged in the water and operated at low speed.

With Assumption 3.1, the off-diagonal components of M_A are considered negligible,

$$M_A = diag([X_{\dot{u}}\ Y_{\dot{v}}\ Z_{\dot{w}}\ K_{\dot{p}}\ M_{\dot{q}}\ N_{\dot{r}}]^T) \tag{6}$$

In skew-symmetric form, the Coriolis-Centripetal matrix due to the added mass is presented as

$$C_A(\nu) = \begin{bmatrix} 0_{3\times3} & [(A_{11}\nu_1 + A_{12}\nu_2)\times] \\ [(A_{11}\nu_1 + A_{12}\nu_2)\times] & [(A_{21}\nu_1 + A_{22}\nu_2)\times] \end{bmatrix} \tag{7}$$

where

$$M_A = \begin{bmatrix} A_{11} & A_{12} \\ A_{21} & A_{22} \end{bmatrix}, \nu_1 = [u\ v\ w]^T, \nu_2 = [p\ q\ r]^T \tag{8}$$

In simplified form, it can be rewritten as

$$C_A(\nu) = -C_A^T(\nu) = \begin{bmatrix} 0 & 0 & 0 & 0 & Z_{\dot{w}}w & -Y_{\dot{v}}v \\ 0 & 0 & 0 & -Z_{\dot{w}}w & 0 & X_{\dot{u}}u \\ 0 & 0 & 0 & Y_{\dot{v}}v & -X_{\dot{u}}u & 0 \\ 0 & Z_{\dot{w}}w & -Y_{\dot{v}}v & 0 & N_{\dot{r}}r & -M_{\dot{q}}q \\ -Z_{\dot{w}}w & 0 & X_{\dot{u}}u & -N_{\dot{r}}r & 0 & K_{\dot{p}}p \\ Y_{\dot{v}}v & -X_{\dot{u}}u & 0 & M_{\dot{q}}q & -K_{\dot{p}}p & 0 \end{bmatrix} \tag{9}$$

The damping due to the viscosity of the fluid medium can be approximated by linear and quadratic terms:

$$D_{R_l} = diag([X_u\ Y_v\ Z_w\ K_p\ M_q\ N_r]^T)$$

$$D_{R_q}(\nu) = diag([X_{u|u|}|u| \; Y_{v|v|}|v| \; Z_{w|w|}|w| \; K_{p|p|}|p| \; M_{q|q|}|q| \; N_{r|r|}|r|]^T) \tag{10}$$

Subsequently, as BlueROV2 Heavy Configuration can be approximately set to neutral buoyancy (e.g. $W - B \approx 0$: approximately zero net force between the weight of BlueROV2 Heavy Configuration and its buoyancy) and by the open-loop inertial state of BlueROV2 Heavy Configuration in Gazebo Physics Engine, $r^b_{B/b}$ can be approximately set as [0, 0, 0.02], the resulting restoring force and moment (due to the gravitational force and buoyancy and their offsets from $\{b\}$) vector can be simplified as follow.

$$g(\eta) = -\begin{bmatrix} R^n_b(\eta)^{-1}(f^n_G + f^n_B) \\ r^b_{G/b} \times R^n_b(\eta)^{-1} f^n_G + r^b_{B/b} \times R^n_b(\eta)^{-1} f^n_B \end{bmatrix}$$
$$= \begin{bmatrix} (W-B)sin(\theta) \\ -(W-B)cos(\theta)sin(\phi) \\ -(W-B)cos(\theta)cos(\phi) \\ [-(y_G W - y_B B)cos(\theta)cos(\phi) \\ +(z_G W - z_B B)cos(\theta)sin(\phi)] \\ [(x_G W - x_B B)cos(\theta)cos(\phi) \\ +(z_G W - z_B B)sin(\theta)] \\ [-(x_G W - x_B B)cos(\theta)sin(\phi) \\ -(y_G W - y_B B)sin(\theta)] \end{bmatrix}$$
$$= \begin{bmatrix} 0 \\ 0 \\ 0 \\ -z_B B cos(\theta)sin(\phi) \\ -z_B B sin(\theta) \\ 0 \end{bmatrix} \tag{11}$$

Given

$$R^n_b(\eta) = R_{z,\psi} R_{y,\theta} R_{x,\phi}$$
$$= \begin{bmatrix} cos(\psi)cos(\theta) & -sin(\psi)cos(\phi) + cos(\psi)sin(\theta)sin(\phi) & sin(\psi)sin(\phi) + cos(\psi)sin(\theta)cos(\phi) \\ sin(\psi)cos(\theta) & cos(\psi)cos(\phi) + sin(\psi)sin(\theta)sin(\phi) & -cos(\psi)sin(\phi) + sin(\psi)sin(\theta)cos(\phi) \\ -sin(\theta) & cos(\theta)sin(\phi) & cos(\theta)cos(\phi) \end{bmatrix} \tag{12}$$

The thruster control matrix (TCM) B is a constant matrix based on the configuration of the thrusters in the UUV body frame $\{b\}$. When the horizontal thrusters are positioned with offsets in all axes from the UUV frame $\{b\}$, all terms in roll and pitch of $B : f_T \rightarrow \tau$ are non-zero and $c_{4i} \ll c_{4j}, c_{5i} \ll c_{5j}$ for $i = \{1, 2, 3, 4\}, j = \{5, 6, 7, 8\}$. For instance, for BlueROV2 Heavy Configuration,

$$B = \begin{bmatrix} c_{11} & c_{12} & c_{13} & c_{14} & 0 & 0 & 0 & 0 \\ c_{21} & c_{22} & c_{23} & c_{24} & 0 & 0 & 0 & 0 \\ 0 & 0 & 0 & 0 & c_{35} & c_{36} & c_{37} & c_{38} \\ c_{41} & c_{42} & c_{43} & c_{44} & c_{45} & c_{46} & c_{47} & c_{48} \\ c_{51} & c_{52} & c_{53} & c_{54} & c_{55} & c_{56} & c_{57} & c_{58} \\ c_{61} & c_{62} & c_{63} & c_{64} & 0 & 0 & 0 & 0 \end{bmatrix} \tag{13}$$

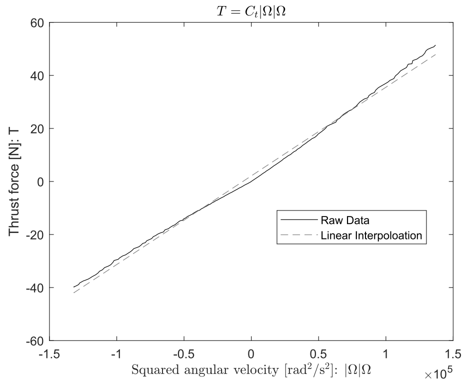

FIGURE 5. Relationship between thrust force and squared angular velocity of T200 thruster.

As B is a non-invertible matrix, the Moore-Penrose Pseudoinverse can be applied to get its inverse,

$$B^{-1} \approx B^{\dagger} = B^T(BB^T)^{-1} \tag{14}$$

which can be used to derive f_T from τ,

$$f_T = B^{\dagger}\tau \tag{15}$$

TCM matrix B only maps the configurations of the thrusters' pose to generate a wrench in the UUV frame $\{b\}$. However, it is necessary to consider the BlueROV2 thruster (T200 model) mapping between the thrust force [N] and squared angular velocity $[\frac{rad^2}{s^2}]$. This mapping can be described as $T = C_t|\Omega|\Omega$ which was mentioned as "basic conversion function" in the UUV simulator ROS project, but in contrast, the plot of the function suggested $T = C_t\Omega$ [43], [49], [50]. Therefore, using the publicly released thruster data from BlueROV2 [51], the actual mapping was plotted as shown in FIGURE 5, generating

$$f_{T_i} = T_i = 0.0003|\Omega_i|\Omega_i + 2.1064 \tag{16}$$

After identifying $C_t = 0.0003$, each component of f_T from Eqn. (15) can be mapped to each thruster's angular velocity by

$$\Omega_i = sgn(f_{T_i})\sqrt{(|f_{T,i}| - 2.1064)/C_t} \tag{17}$$

where $i = \{1, 2, 3, 4, 5, 6, 7, 8\}$ and $|f_{T_i}| = |T_i| \geq 2.1064$

The time constant (0.0112 s) of the first-order model of the T200 thruster is decided via the MATLAB system identification app [52].

Lastly, $\tau_{current}$ can be applied as a wrench disturbance input in the Gazebo Physics Engine.

$$\tau_{current} = \begin{bmatrix} f_{x_{disturb}} \\ f_{y_{disturb}} \\ f_{z_{disturb}} \\ m_{x_{disturb}} \\ m_{y_{disturb}} \\ m_{z_{disturb}} \end{bmatrix} \tag{18}$$

Although $\tau_{current}$ seems easy to be added as a disturbance, measuring the underwater current is more feasible in the actual deployment. Therefore, in Section: VI, the underwater current velocity will be taken as the disturbance instead of $\tau_{current}$.

System parameter (e.g., added mass, linear and quadratic damping) estimations are referred from the experiments on BlueROV2 Heavy Configuration and listed in TABLE 3 [53]. As the values of linear and quadratic damping coefficients for roll, pitch and yaw make BlueROV2 Heavy Configuration open-loop-unstable in Gazebo Physics Engine, those parameter values are readjusted until the system is approximately open-loop-stable in the Gazebo Physics Engine around the operating speed of 0.28 m/s.

TABLE 3. System parameters of BlueROV2 heavy configuration.

Parameters	Value	Unit
m	11.5	[kg]
W	112.8	[N]
B	112.9	[N]
x_G, y_G, z_G	0,0,0	[m]
x_B, y_B, z_B	0,0,0.02	[m]
$I_{xx}, I_{yy}, I_{zz}, \ldots$	0.21,0.18,0.31,0,...	[kg m^2]
X_u, Y_v, Z_w	4.03, 6.22, 5.18	[N s/m]
K_p, M_q, N_r	4.53, 4.4, 3.13	[N m s/rad]
$X_{u\|u\|}, Y_{v\|v\|}, Z_{w\|w\|}$	18.18, 21.66, 36.99	[N s^2/m^2]
$K_{p\|p\|}, M_{q\|q\|}, N_{r\|r\|}$	26.32, 26.9, 24.63	[N m s^2/rad^2]
$X_{\dot{u}}, Y_{\dot{v}}, Z_{\dot{w}}$	5.5, 12.7, 14.57	[kg]
$K_{\dot{p}}, M_{\dot{q}}, N_{\dot{r}}$	3.77, 3.77, 3.77	[kg m^2]

IV. FORMULATION OF VISUAL INSPECTION TASK SCENARIO

To be as realistic and practical as the actual deployment of UUVs in offshore aquaculture, it is imperative to gather as many available parameters as possible for the farm and physical constraints. In this simulation study, the Blue Endeavour site by the New Zealand King Salmon company will be conceptualized as the visual inspection task scenario [56]. It is located 5 kilometres due north of Cape Lambert, in northern Marlborough. The proposed Blue Endeavour site consists of two blocks, each comprising two by five circular floating flexible fish net-pens. The main specifications of the site and the inspection task are listed in TABLE 4.

It is assumed that the UUV follows a helical trajectory about 4 m away from the fish net-pen. Upon completing the task, the UUV returns to the docking station in the shortest path. The visual inspection task will be conducted only at each fish net-pen out of ten at one time. The mean underwater current speed is within 0.5 m/s below 10 m depth and the surface mean current speed can reach up to 0.9 m/s [55, p.16].

As shown in TABLE 4, a UUV for the visual inspection in the Blue Endeavour site needs to generate a minimum surge, sway and heave velocity of 0.768 m/s and operate continuously for at least two hours.

A. VISUAL INSPECTION TRAJECTORY

The visual inspection process is indeed a visual full-area coverage problem which can be explained as shown in FIGURE 6. The viewable frame defined by width W and height H at a certain distance d_{gap} will overlap the consecutive camera frame which subsequently must overlap the following camera frame when BlueROV2 Heavy Configuration reaches 2^{nd} helical turn. In fact, the overlapping height H_O and the viewable frame height H will determine the helical pitch p.

Using the horizontal field of view (HFOV) β and vertical FOV (VFOV) α, width W and height H can be calculated.

$$\begin{aligned} H &= 2d_{gap} \tan(\alpha/2) \\ W &= 2d_{gap} \tan(\beta/2) \end{aligned} \tag{22}$$

The required pitch p can be calculated using H and H_O

$$p = H - H_O \tag{23}$$

Upon identifying pitch p, d_{travel} from TABLE 4 can be calculated, and with the user input of the allowable inspection time t, the ideal average velocity to complete the task v_a can be computed. Finally, the resulting v can be validated whether it is lower than the operating velocity of BlueROV2 Heavy Configuration ensuring that the UUV has the capacity to follow the trajectory and complete fish net-pen visual inspection in the specified duration.

For instance, β is 80 deg for BlueROV2's Low-Light HD USB camera resulting $W = 6.71$ m. $H = 3.77$ m can be determined by the aspect ratio (1920 × 1080 2MP 16:9). By setting $H_O = 2.27$ m, the helical pitch p is resulted as 1.5 m. For the 15 m depth fish net-pen and in consideration of 2 h (120 min), TABLE 4 provides detailed calculation and without average underwater current, the minimum required velocity to complete the task can be evaluated as 0.268 m/s.

Remark 4.1: A 4 DoF (surge, sway, heave, and yaw) helical trajectory is generated for 6 DoF BlueROV2 Heavy Configuration to perform fish net-pen visual inspection.

V. TRAJECTORY TRACKING CONTROLLER

Prior to the development of the controller, several additional terms as shown in TABLE 5, are defined for the space transformation between frame $\{n\}$ and frame $\{b\}$.

The transformation matrix $J_b^n(\eta)$, to map the velocity from frame $\{b\}$ to frame $\{n\}$ is defined:

$$\dot{\eta} = J_b^n(\eta)\nu \tag{24}$$

where

$$\begin{aligned} J_b^n(\eta) &= \begin{bmatrix} R_b^n(\eta) & 0_{3\times3} \\ 0_{3\times3} & T_b^n(\eta) \end{bmatrix}, \\ J_n^b(\eta) &= \begin{bmatrix} R_b^n(\eta)^{-1} & 0_{3\times3} \\ 0_{3\times3} & T_b^n(\eta)^{-1} \end{bmatrix} \end{aligned} \tag{25}$$

and

$$T_b^n(\eta) = \begin{bmatrix} 1 & sin(\phi)tan(\theta) & cos(\phi)tan(\theta) \\ 0 & cos(\phi) & -sin(\phi) \\ 0 & sin(\phi)/cos(\theta) & cos(\phi)/cos(\theta) \end{bmatrix}, \theta \neq \pm\frac{\pi}{2} \tag{26}$$

TABLE 4. Specifications of Blue Endeavour site by the New Zealand King Salmon company.

Description	Parameter	Value	Notes
Internal diameter of fish net-pen	D	53.5 m	Initial development [54, p.7]
Height (Depth) of fish net-pen	h	15 m	This is provided by the New Zealand King Salmon company
Distance to travel(helical length)	d_{travel}	1932 m	Pitch: $p = 1.5$ Gap between UUV and fish net-pen: $d_{gap} = 4\,\text{m}$ Number of turns: $n = h/p = 10$ $$d_{travel} = n\sqrt{\pi^2(D + 2d_{gap})^2 + p^2} \quad (19)$$
Allowable inspection time	t	2 h	This is inferred from [11].
Average underwater current	v_c	0.5 m/s	This is based on [55, p.16].
Average velocity (ideal) to complete the task	v_a	0.268 m/s	$$v_a = d_{travel}/t \quad (20)$$
Min. required velocity to complete the task	v	0.768 m/s	This is the minimum velocity required by BlueROV2 Heavy Configuration in the desired direction upon encountering the average underwater current reported in [55, p.16]. It is not directly related to the controller output velocity. $$v = v_c + v_a \quad (21)$$

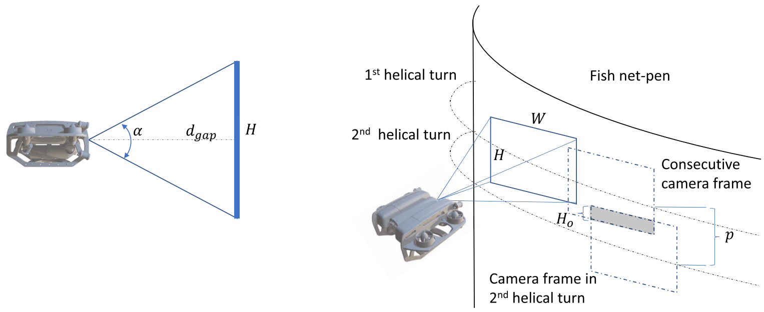

FIGURE 6. (Left) Illustration of camera parameters. (Right) Visual full-area coverage problem.

$$T_n^b(\eta) = T_b^n(\eta)^{-1} = \begin{bmatrix} 1 & 0 & -sin(\theta) \\ 0 & cos(\phi) & sin(\phi)cos(\theta) \\ 0 & -sin(\phi) & cos(\phi)cos(\theta) \end{bmatrix} \quad (27)$$

Compensated-PD, Compensated-PID and CTC/IDC control schemes can be applied to achieve trajectory tracking by the UUV. Here the terms for compensation are restoring force and moment to be more precise and concrete.

A. GAIN TUNINGS FOR COMPENSATED-PD AND COMPENSATED-PID

In the UUV's trajectory tracking controller for Compensated-PD and Compensated-PID, τ in Eqn. (1) can be injected as [47, p. 375]

$$\tau = g(\eta) + J_n^b(\eta)\tau_{PID} \quad (28)$$

where

$$\tau_{PID} = K_p e + K_i \int_0^t e\,dt + K_d \dot{e} \quad (29)$$

For PID gain tunings on Compensated-PD and Compensated-PID, it is on a trial and error basis.

Remark 5.1: As shown in Eqn. (28), when the error approaches zero or becomes zeros, the UUV's motion attenuates. $g(\eta)$ from Eqn. (11) clearly indicates that it has no effects on surge, sway and heave but only on roll, pitch and yaw.

Remark 5.2: As eight thrusters maneuver a 6-DoF UUV, gains are not independent across surge, sway, heave, roll, pitch and yaw. Specifically, surge, sway and yaw are dependent. Similarly, roll, pitch and heave are dependent.

B. GAIN TUNINGS FOR CTC/IDC

Define the tracking acceleration error:

$$\ddot{e} \triangleq \ddot{\tilde{\eta}} = \ddot{\eta}_d - \ddot{\eta} \quad (30)$$

By the use of $J_n^b(\eta)$, Eqn. (30) becomes

$$J_n^b(\eta)\ddot{\tilde{\eta}} = J_n^b(\eta)\ddot{\eta}_d - J_n^b(\eta)\ddot{\eta} \quad (31)$$

TABLE 5. Additional terms to describe error in different frames.

Terms	Descriptions
$\eta_d = [x_d\ y_d\ z_d\ \phi_d\ \theta_d\ \psi_d]^T \in \mathbb{R}^6$	: desired position and orientation (Euler angles) vector w.r.t frame $\{n\}$ expressed in frame $\{n\}$
$e \triangleq \tilde{\eta} = \eta_d - \eta = [e_x\ e_y\ e_z\ e_\phi\ e_\theta\ e_\psi]^T$	: pose tracking error w.r.t frame $\{n\}$ expressed in frame $\{n\}$
$\dot{e} \triangleq \dot{\tilde{\eta}} = \dot{\eta}_d - \dot{\eta} = [e_u\ e_v\ e_w\ e_p\ e_q\ e_r]^T$	: twist tracking error w.r.t $\{n\}$ expressed in frame $\{n\}$
$J_b^n(\eta) \neq J_b^n(\eta)^{-1}$	: transformation from frame $\{b\}$ to frame $\{n\}$ using Euler angles.

Computed torque is designed in the form of

$$\tau = M(J_n^b(\eta)\ddot{\eta}_d - f_F) + (C(\nu) + D(\nu))\nu + g(\eta) \quad (32)$$

where f_F is the feedback control loop.

Remark 5.3: As shown in Eqn. (32), unless the term: $M(J_n^b(\eta)\ddot{\eta}_d - f_F)$ overwhelmingly dominates in τ, there is an effect of the UUV's dynamics on the control.

Substituting Eqn. (32) in Eqn. (1), we have

$$\begin{aligned} M\dot{\nu} + (C(\nu) + D(\nu))\nu + g(\eta) \\ = M(J_n^b(\eta)\ddot{\eta}_d - f_F) + (C(\nu) + D(\nu))\nu + g(\eta) \\ \dot{\nu} = J_n^b(\eta)\ddot{\eta}_d - f_F \\ f_F = J_n^b(\eta)(\ddot{\eta}_d - \ddot{\eta}) = J_n^b(\eta)\ddot{e} \end{aligned} \quad (33)$$

Now, we can design f_F such that the tracking error converges to zero by choosing

$$f_F = -J_n^b(\eta)\tau_{PID} \quad (34)$$

Therefore, Eqn. (33) becomes

$$\begin{aligned} -J_n^b(\eta)\tau_{PID} = J_n^b(\eta)\ddot{e} \\ \dddot{e} + K_d\ddot{e} + K_p\dot{e} + K_i e = 0 \end{aligned} \quad (35)$$

As the error dynamics of CTC/IDC is a third-order system, its characteristic equation (CE) can be expressed as the product of the CE of a second-order system determined by two dominant poles and the CE of a first order system [57, Chapter 11.2], [58, p. 618],

$$\begin{aligned} s^3 + K_d s^2 + K_p s + K_i &= (s^2 + 2\zeta\omega_n s + \omega_n^2)(s + s_0) \\ &= s^3 + (2\zeta\omega_n + s_0)s^2 + \\ &\quad + (2\zeta\omega_n s_0 + \omega_n^2)s + \omega_n^2 s_0 \end{aligned} \quad (36)$$

where ζ and ω_n are the damping ratio and natural frequency of the second order system, $-s_0$ is the pole of the first-order system.

Using the pole placement technique for a second-order system, the control gains are given by

$$K_p = 2\zeta\omega_n s_0 + \omega_n^2 \quad (37)$$

$$K_i = \omega_n^2 s_0 \quad (38)$$

$$K_d = 2\zeta\omega_n + s_0 \quad (39)$$

By analyzing through Routh-Hurwitz stability criterion, it is obvious that the tracking error converges to zero asymptotically when $K_p > 0$, $K_d > 0$, $K_i > 0$ and $K_p K_d > K_i$.

Although the nonlinear terms are canceled out in CTC/IDC, it is worth noting that Remark 5.2 is still applicable as thrusts of eight thrusters are mapped via $B^\dagger$ using the controller output τ according to Eqn. (15). In other words, all DoF in τ are uncoupled, but the resulting thrusts of horizontal thrusters are coupled among surge, sway and yaw and those of vertical thrusters are coupled among roll, pitch and heave.

Remark 5.4: K_p always results in a steady-state error. Introducing K_i to the controller minimizes/ eliminates the steady-state error, but a large K_i makes the system response oscillatory. K_d improves the closed-loop stability by increasing damping but has opposite effects with a large K_d [59, Chapter 3.3].

Remark 5.5: The selection of ζ, ω_n and s_0 are crucial for the weight of the term $M(J_n^b(\eta)\ddot{\eta}_d - f_F)$ in τ. As mentioned in Remark 5.3, it will also affect the role of the UUV dynamic model in the control. In this work, CTC/IDC will be designed to keep the effect of the UUV dynamic model as a unique feature in contrast to Compensated-PID.

C. ANTI-WINDUP ALGORITHM FOR INTEGRATOR

It is observed that large errors due to the system dynamics in CTC/IDC are accumulated through the integrator in the controller,

$$I_j = K_i \int_0^t e_j\, dt \quad (40)$$

where e_j and I_j are the tracking error and the integral term respectively corresponding to the j^{th} element of τ, and K_i is the integral control gain. In the worst case, it makes the control input τ saturated and less effective to eliminate tracking errors (especially rotational tracking errors) [59, p. 80].

Therefore, it is adjusted through the following anti-windup mechanism,

$$I_j = \begin{cases} sgn(I_j)L_j & \text{if } I_j > L_j \\ I_j & \text{if } I_j < L_j \\ 0 & \text{if } |e_j| < \epsilon \end{cases} \quad (41)$$

where $j = \{1, 2, 3, 4, 5, 6\}$. L_j and ϵ are the anti-windup limits tabulated in TABLE 6. They are decided from the empirical results.

VI. EXPERIMENTAL HIGH-FIDELITY SIMULATION STUDY

To observe the physics effects, Gazebo was integrated with ROS such that the controller outputs from ROS drive BlueROV2 Heavy Configuration in Gazebo from which odometry data is published to ROS.

TABLE 6. Anti-windup limits.

	L_1	L_2	L_3	L_4	L_5	L_6	ϵ
Limit	17.65 N	17.65 N	24.96 N	7 N m	7 N m	7 N m	0.01

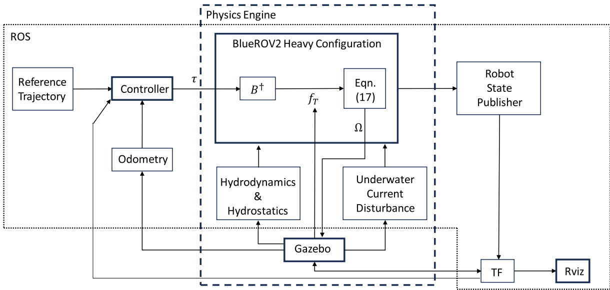

FIGURE 7. Simplified block diagram of ROS-Gazebo communication.

FIGURE 7 shows the simplified block diagram of the communications among the components of ROS and Gazebo, and the detailed explanations are reported in [44]. Gazebo plugins in ROS create hydrodynamic & hydrostatic effects from TABLE 3, thrusts & angular velocities of T200 thrusters from Eqn. (15) and Eqn. (17) respectively and underwater current disturbances from TABLE 9. Moreover, it publishes the odometry data of BlueROV2 Heavy Configuration via navigation message in ROS. The proposed ROS controllers use the odometry data and reference trajectory as the inputs and generate the forces and moments as the outputs. Robot State Publisher broadcasts the 3D poses of the frames in BlueROV2 Heavy Configuration to TF which is a ROS package, carrying out coordinate frame transformation. Therefore, via TF, coordinate frame transformations among multiple different frames with timestamps are accessible in ROS as long as those frames are under the ROS TF frame tree [60]. All these frame transformations, reference trajectory, underwater current disturbance marker and camera feedback can be visualized in the ROS visualization tool called Rviz [61].

In addition to the BlueROV2 Heavy Configuration, other objects such as the ocean floor and fish net-pen (treated as a static object in this work) can be defined at the desired location in Gazebo. Moreover, the collision feature can be added to the fish net-pen if required and to minimize the computation load, this feature is not used in this work. According to the fish farm size as shown in TABLE 4, Collada file formats are generated via Blender software and imported in Gazebo as shown in FIGURE 8 [62]. Although the suggested mesh size in the Blue Endeavour project is 35 mm, generating thousands of such a small mesh size is computationally intensive and thus, the fish net-pen was modeled with 100 mm mesh size as shown in FIGURE 9.

A. SIMULATION PARAMETERS: BLUEROV2 HEAVY CONFIGURATION

It is important to set the simulation parameters as close to the value experimentally evaluated to minimize any potential

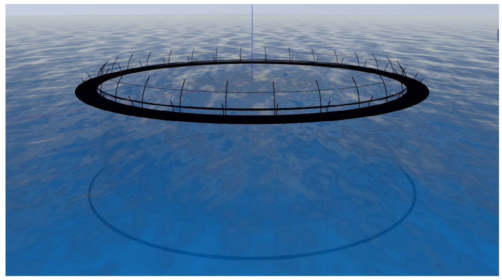

FIGURE 8. Isometric view of Blue Endeavour fish farm (Artist impression).

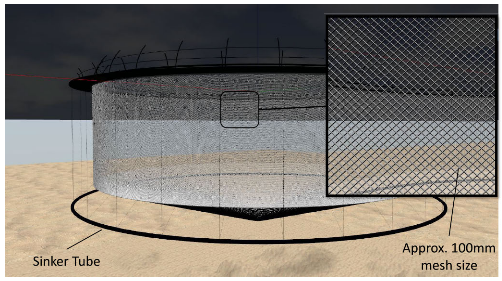

FIGURE 9. Side view of Blue Endeavour fish farm (Artist impression).

discrepancy. A rotor constant of 0.0003, experimentally identified parameter as shown in Eqn. (16) and a maximum thrust limit of 45.67 N—the average value between maximum forward and reverse thrust—are determined from the publicly available dataset of T200 thruster used in BlueROV2 Heavy Configuration [51]. For BlueROV2 Heavy Configuration with horizontal thrusters in the 45 degree vectored formation, the maximum control thrust is 88.25 N for surge, sway, and is 137 N for heave [37]. Using Eqn. (15) with a surge force of 88.25 N, the maximum rated thrust of 31.25 N for the T200 thruster is derived. Note: to avoid representation singularity, Euler angles are transformed into quaternion for the actual implementation in ROS.

B. SIMULATION PARAMETERS: CONTROLLER

It is important to know the control saturation of each DoF of the UUV so that the controller outputs can be constrained properly. One quick way to find it for each DoF is to activate the respective thruster at its maximum rated thrust of 31.25 N at the correct thrust direction from

$$\tau = Bf_T \tag{42}$$

The resulting control saturation values (S_{c_i}) are reported in TABLE 7 where $i = \{1, 2, 3, 4, 5, 6\}$. These control saturation values are imposed on the controller outputs $\tau = [X, Y, Z, K, M, N]^T$.

$$-S_{c_i} \leq \tau_i \leq S_{c_i} \tag{43}$$

which makes each T200 thruster output be constrained by its maximum rated thrust of 31.25 N.

$$-31.25\,\mathrm{N} \le f_{T_i} \le 31.25\,\mathrm{N} \tag{44}$$

The next step is to detail the selection of ζ, ω_n and s_0. For CTC/IDC gain tunings, to minimize oscillations at the expense of a slow response for safety purpose [41], [63], one possible choice for a particular DoF of CTC/IDC is

$$\zeta = 1.1$$

Using the chosen ζ with the additional choice of s_0, Eqn. (37) to (39) can be computed for a particular DoF of CTC/IDC as long as the CE of the second-order system has two dominant poles.

$$-s_0 \ll -\zeta\omega_n \pm \omega_n\sqrt{\zeta^2 - 1} \tag{45}$$

$$s_0 \gg \zeta\omega_n \mp \omega_n\sqrt{\zeta^2 - 1} \tag{46}$$

In addition to this first condition, to fulfill Remark 6.2, there are two more conditions.

The second condition is

$$\frac{K_d}{K_i} = \frac{k + s_0}{\omega_n^2 s_0} > 1 \rightarrow s_0 > \frac{-k}{1 - \omega_n^2} \tag{47}$$

However,

$$s_0 > 0 \rightarrow s_0 > \frac{k}{1 - \omega_n^2} \tag{48}$$

$$\omega_n < 1 \tag{49}$$

The third condition is

$$\frac{K_p}{K_d} = \frac{ks_0 + \omega_n^2}{k + s_0} > 1 \rightarrow s_0 > \frac{k - \omega_n^2}{k - 1} \tag{50}$$

$$s_0 > 0 \rightarrow \frac{1}{2\zeta} < \omega_n < 2\zeta \tag{51}$$

where $k = 2\zeta\omega_n$. Among three conditions on s_0 resulting from Eqn. (46), Eqn.(48) and Eqn. (50), the strict condition is the first one and the remaining s_0 conditions are relatively flexible.

For instance, using the chosen ζ and $\omega_n = 0.5$ and to fulfill all three s_0 conditions,

$$s_0 > 8.5$$

However, s_0 of 8.5 will result in very large PID gains for CTC/IDC and thus, CTC/IDC controller output along with the canceling nonlinear terms in CTC/IDC will approach to control saturation values reported in TABLE 7.

Therefore, complying with the first s_0 condition and relaxing on the last condition, select

$$s_0 = 1.5$$

Remark 6.1: The selection of ζ, ω_n and s_0 is not unique. However, the selection should adhere to the conditions mentioned above.

Remark 6.2: Generally, PID gains, in this work, will be set such that K_p is larger than K_d and K_d is larger than K_i unless specified due to the behaviours of PID mentioned in Remark 5.4.

So far, the selection of ζ, ω_n and s_0 of a particular DoF of CTC/IDC has been presented. The next step is how to decide those parameters for the remaining DoFs. The proposed method is to utilize properties of the UUV dynamic model because of the physical coupling of eight thrusters as mentioned in Remark 5.2. Among the UUV parameters as shown in TABLE 3, the quadratic damping coefficients are relatively higher than other parameters and thus, potentially the ratios of those coefficients can provide the weighted values for ζ and ω_n and s_0 of each DoF.

By taking the surge motion as the baseline and using the previously chosen ζ, ω_n and s_0,

$$\zeta_x = \zeta$$
$$\omega_{n_x} = \omega_n$$
$$s_{0_x} = s_0$$

Using the ratio of quadratic damping coefficients, the parameters for sway can be decided by

$$\zeta_y = \frac{Y_{v|v|}}{X_{u|u|}}\zeta_x \tag{52}$$

$$\omega_{n_y} = \frac{X_{u|u|}}{Y_{v|v|}}\omega_{n_x} \tag{53}$$

$$s_{0_y} = \frac{Y_{v|v|}}{X_{u|u|}}s_{0_x} \tag{54}$$

Similarly, the parameters of the remaining DoF can be decided with the respective quadratic damping coefficients. The DoF subscripts (e.g., x, y) of ζ and ω_n and s_0 are removed in TABLE 8.

Remark 6.3: The tuning method only provides a general guideline, but readjusting gain values is required according to the experimental results. For instance, K_p and K_i for roll, pitch and yaw of CTC/IDC are further fine-tuned as the UUV has oscillations using the default tuned values.

Other critical controller parameters such as anti-windup limits, control saturation values and the control gains and tuning parameters for Compensated-PD, Compensated-PID and CTC/IDC are tabulated from TABLEs 6 to 8 respectively.

C. SIMULATION PARAMETERS: INITIAL POSITION OF THE UUV

As the inertial frame or a global reference frame, frame $\{n\}$ is defined at the center of the fish net-pen at the ocean surface. Subsequently, BlueROV2 Heavy Configuration is initially put in frame $\{n\}$ at $x = 30.75$ m—considering the 4 m gap between the UUV and fish net-pen, $y = 0$ m, $z = 0$ m and $\psi = \pi$ rad so that it faces tangential to the circumference of the fish net-pen.

TABLE 7. Control saturation values.

	Surge (x)	Sway (y)	Heave (z)	Roll (ϕ)	Pitch (θ)	Yaw (ψ)
S_{c_i}	$88.25\,\mathrm{N}$	$88.255\,\mathrm{N}$	$127\,\mathrm{N}$	$31\,\mathrm{N\,m}$	$14\,\mathrm{N\,m}$	$21\,\mathrm{N\,m}$

TABLE 8. Control gains and tuning parameters for the controllers.

Controller	Gain	x	y	z	ϕ	θ	ψ
Compensated-PD	K_p	5	5.957	10.173	7.239	7.398	6.774
	K_d	4.545	5.415	9.248	6.581	6.725	6.158
Compensated-PID	K_p	5	5.957	10.173	7.239	7.398	6.774
	K_i	1.136	0.954	0.558	0.785	0.768	0.839
	K_d	4.545	5.415	9.248	6.581	6.725	6.158
CTC/IDC	K_p	1.9	2.142	3.418	8.508	8.556	8.372
	K_i	0.375	0.315	0.184	0.459	0.453	0.477
	K_d	2.6	2.887	4.152	3.272	3.319	3.132
	s_0	1.5	1.79	3.05	2.17	2.22	2.03
	ζ	1.1	1.31	2.24	1.59	1.63	1.49
	ω_n	0.5	0.42	0.25	0.35	0.34	0.37

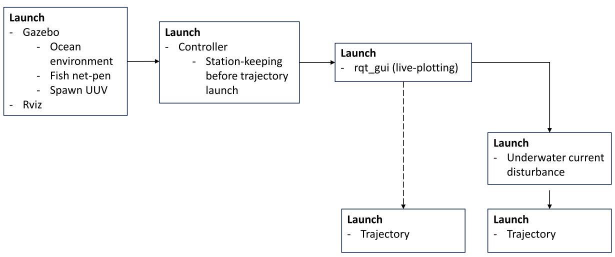

FIGURE 10. ROS simulation launch procedure.

D. SIMULATION PARAMETERS: TRAJECTORY

Afterward, the 4 DoF (surge, sway, heave and yaw) helical trajectory is initiated at the same starting point as the UUV with number of waypoints: $wp = 4000$ points, number of turns: $n = 10$, depth: $h = 15\,\mathrm{m}$, allowable inspection time: $t = 2\,\mathrm{h}$, maximum forward speed of $0.28\,\mathrm{m/s}$, and heading angle offset of $\pi/2$ rad.

E. SIMULATION PARAMETERS: UNDERWATER CURRENT DISTURBANCES

Assumption 6.1: As the fish net-pen is relatively very small in the vast ocean surface, the current disturbance is assumed to be an irrotational constant flow.

As mentioned in TABLE 4, the average underwater current speed is $0.5\,\mathrm{m/s}$ and the mean current speed can reach up to $0.9\,\mathrm{m/s}$. In this work, three different scenarios of disturbances will be experimented as shown in TABLE 9. The underwater current is constantly flowing in the direction of the x-axis of the frame $\{n\}$ throughout the whole experiment. In other words, BlueROV2 Heavy Configuration experiences the current disturbance at all times.

The aforementioned simulation parameters are set up for each controller and the ROS simulation launch procedure is provided in FIGURE 10. Approximately a 2-hour long simulation video for each controller is recorded with, live-plotting of error: e, $\dot{e}$ as defined in TABLE 5, f_T and τ along with Rviz visualization widget (displaying camera-view of the UUV, the helical trajectory, and reference frames) and Gazebo (displaying the fish net-pen and the UUV). Note: orientation error in quaternion is converted to Euler angles for ease of visualization in live-plotting.

VII. HIGH-FIDELITY SIMULATION RESULTS AND DISCUSSION

In this section, the discussion will be targeted to the comparative performance of CTC/IDC, Compensated-PID and Compensated-PD in terms of trajectory tracking, overall performance and finally advantages and drawbacks of CTC/IDC. All three controllers were tested in three current disturbance scenarios as shown in TABLE 9. However, the discussion will highlight the current disturbance scenario of $0.5\,\mathrm{m/s}$ and $0.9\,\mathrm{m/s}$ as that of $0.0\,\mathrm{m/s}$ is too idealistic in the physical world. For the quantitative analysis, the numerical results such as root-mean-squared-error (RMSE), mean-absolute-error (MAE) and root-sum-squared (RSS) were reported.

$$RMSE = \sqrt{\frac{\Sigma_{i=0}^{N} e_i^2}{N}} \tag{55}$$

$$MAE = \frac{\Sigma_{i=0}^{N} |e_i|}{N} \tag{56}$$

$$RSS = \sqrt{\Sigma_{i=0}^{N} e_i^2} \tag{57}$$

where e_i refer to both e and $\dot{e}$. In addition, histogram & normal distribution fitting, bar charts and plots were utilized to portray the results graphically.

The simulation videos are available at this hyper link. All tracking error plots with respect to time show the excitation of the signals at a different time as it takes a slightly different duration of time to load the Gazebo Physics Engine with large files such as the fish net-pen at each simulation. Therefore, only after the Gazebo's loading is finished, the helical trajectory is generated.

TABLE 9. Current disturbance scenarios.

Scenarios	Current	Direction	Duration
S1: No disturbance	$0\,\mathrm{m/s}$	Horizontal: x-axis of frame $\{n\}$	Full
S2: Medium disturbance	$0.5\,\mathrm{m/s}$	Horizontal: x-axis of frame $\{n\}$	Full
S2: Large disturbance	$0.9\,\mathrm{m/s}$	Horizontal: x-axis of frame $\{n\}$	Full

TABLE 10. Trajectory Tracking — root-mean-square-error (RMSE), mean-absolute-error (MAE) and root-sum-squared (RSS).

		S1: Disturbance $(0.0\,\mathrm{m/s})$			**S2: Disturbance** $(0.5\,\mathrm{m/s})$			**S3: Disturbance** $(0.9\,\mathrm{m/s})$		
		CTC/IDC	**Compensated-PID**	**Compensated-PD**	**CTC/IDC**	**Compensated-PID**	**Compensated-PD**	**CTC/IDC**	**Compensated-PID**	**Compensated-PD**
e_x	RMSE	6.11e-03	1.64e-01	4.01e-01	7.64e-02	5.16e-01	1.37e+00	1.83e-01	1.64e+00	3.58e+00
	MAE	4.76e-03	1.31e-01	3.60e-01	6.90e-02	3.97e-01	1.21e+00	1.54e-01	1.31e+00	3.28e+00
	RSS	4.02e+00	1.08e+02	2.67e+02	5.00e+01	3.41e+02	9.03e+02	1.20e+02	1.09e+03	2.37e+03
e_y	RMSE	1.74e-02	1.65e-01	4.05e-01	3.65e-02	2.34e-01	5.60e-01	5.34e-02	4.70e-01	8.11e-01
	MAE	5.05e-03	1.30e-01	3.63e-01	1.28e-02	1.74e-01	4.72e-01	2.85e-02	3.50e-01	6.92e-01
	RSS	1.14e+01	1.09e+02	2.69e+02	2.39e+01	1.55e+02	3.70e+02	3.51e+01	3.12e+02	5.38e+02
e_z	RMSE	6.38e-03	2.58e-02	1.66e-02	1.35e-02	1.37e-01	1.41e-01	3.93e-02	4.35e-01	3.89e-01
	MAE	3.83e-03	2.05e-02	1.52e-02	9.69e-03	6.90e-02	9.62e-02	2.86e-02	2.32e-01	3.16e-01
	RSS	4.20e+00	1.71e+01	1.11e+01	8.81e+00	9.05e+01	9.33e+01	2.58e+01	2.88e+02	2.58e+02
e_ϕ	RMSE	2.16e+01	8.99e+00	5.78e+00	4.39e+01	1.60e+01	2.73e+01	7.23e+01	3.72e+01	4.74e+01
	MAE	1.96e+01	7.71e+00	5.74e+00	3.11e+01	9.87e+00	1.84e+01	5.79e+01	2.34e+01	3.74e+01
	RSS	1.42e+04	5.95e+03	3.85e+03	2.87e+04	1.06e+04	1.80e+04	4.74e+04	2.47e+04	3.14e+04
e_θ	RMSE	6.35e+00	4.44e+00	2.41e+00	2.57e+01	1.37e+01	2.09e+01	3.84e+01	2.50e+01	2.50e+01
	MAE	5.35e+00	3.04e+00	1.13e+00	2.06e+01	9.63e+00	1.52e+01	3.14e+01	1.80e+01	1.86e+01
	RSS	4.18e+03	2.94e+03	1.60e+03	1.68e+04	9.04e+03	1.38e+04	2.52e+04	1.66e+04	1.65e+04
e_ψ	RMSE	1.41e+01	7.10e+00	1.47e+00	2.31e+01	1.34e+01	1.77e+01	5.45e+01	2.41e+01	2.91e+01
	MAE	1.19e+01	5.74e+00	9.58e-01	1.71e+01	8.55e+00	1.37e+01	4.10e+01	1.41e+01	1.98e+01
	RSS	9.32e+03	4.70e+03	9.81e+02	1.51e+04	8.89e+03	1.17e+04	3.58e+04	1.60e+04	1.93e+04
e_u	RMSE	4.04e-03	4.84e-02	4.62e-03	2.79e-02	9.84e-02	1.58e-02	6.20e-02	1.30e-01	4.02e-02
	MAE	2.44e-03	3.88e-02	3.48e-03	1.91e-02	7.58e-02	1.06e-02	4.23e-02	1.01e-01	2.79e-02
	RSS	2.66e+00	3.20e+01	3.08e+00	1.82e+01	6.51e+01	1.05e+01	4.07e+01	8.65e+01	2.67e+01
e_v	RMSE	1.12e-02	4.92e-02	7.29e-03	3.04e-02	7.68e-02	2.38e-02	4.97e-02	1.25e-01	6.01e-02
	MAE	2.56e-03	3.92e-02	3.60e-03	1.54e-02	5.73e-02	1.63e-02	3.52e-02	9.42e-02	4.21e-02
	RSS	7.37e+00	3.25e+01	4.86e+00	1.99e+01	5.08e+01	1.57e+01	3.26e+01	8.32e+01	3.99e+01
e_w	RMSE	4.38e-03	1.21e-02	3.58e-03	2.02e-02	5.83e-02	2.84e-02	5.15e-02	1.10e-01	6.38e-02
	MAE	2.28e-03	9.44e-03	3.16e-03	1.39e-02	3.69e-02	1.95e-02	3.72e-02	8.00e-02	4.44e-02
	RSS	2.88e+00	8.03e+00	2.39e+00	1.32e+01	3.85e+01	1.88e+01	3.38e+01	7.28e+01	4.23e+01
e_p	RMSE	1.55e+01	8.93e+00	2.24e+00	1.51e+02	8.01e+01	9.44e+01	3.80e+02	2.20e+02	2.84e+02
	MAE	9.21e+00	4.65e+00	9.13e-01	8.75e+01	4.10e+01	4.67e+01	2.71e+02	1.36e+02	1.87e+02
	RSS	1.02e+04	5.91e+03	1.49e+03	9.88e+04	5.30e+04	6.24e+04	2.49e+05	1.46e+05	1.89e+05
e_q	RMSE	1.06e+02	9.95e+01	3.90e+01	3.96e+02	3.28e+02	2.91e+02	8.01e+02	6.98e+02	7.02e+02
	MAE	7.52e+01	7.67e+01	2.40e+01	2.60e+02	2.17e+02	1.98e+02	5.98e+02	5.19e+02	5.46e+02
	RSS	6.95e+04	6.58e+04	2.60e+04	2.59e+05	2.17e+05	1.93e+05	5.26e+05	4.63e+05	4.66e+05
e_r	RMSE	1.07e+02	1.11e+02	3.72e+01	4.11e+02	4.24e+02	3.52e+02	8.17e+02	8.22e+02	7.67e+02
	MAE	8.13e+01	8.29e+01	2.85e+01	2.71e+02	2.68e+02	2.39e+02	6.12e+02	6.09e+02	6.09e+02
	RSS	7.05e+04	7.32e+04	2.48e+04	2.69e+05	2.80e+05	2.33e+05	5.36e+05	5.45e+05	5.09e+05

TABLE 11. Trajectory Tracking — pose mean-absolute-error (MAE) ratio-comparison across CTC/IDC, Compensated-PID and Compensated-PD tested in simulated underwater current disturbances. Note: CTC/IDC is taken as the baseline for comparison in each disturbance scenario.

		S1: Disturbance $(0.0\,\mathrm{m/s})$			**S2: Disturbance** $(0.5\,\mathrm{m/s})$			**S3: Disturbance** $(0.9\,\mathrm{m/s})$		
		CTC/IDC	**Compensated-PID**	**Compensated-PD**	**CTC/IDC**	**Compensated-PID**	**Compensated-PD**	**CTC/IDC**	**Compensated-PID**	**Compensated-PD**
MAE	e_x	1.00	2.74e+01	7.57e+01	1.00	5.75	1.76e+01	1.00	8.49	2.13e+01
	e_y	1.00	2.58e+01	7.19e+01	1.00	1.37e+01	3.70e+01	1.00	1.23e+01	2.43e+01
	e_z	1.00	5.35	3.96	1.00	7.11	9.92	1.00	8.13	1.10e+01
	e_ϕ	1.00	0.39	0.29	1.00	0.32	0.59	1.00	0.40	0.65
	e_θ	1.00	0.57	0.21	1.00	0.47	0.74	1.00	0.57	0.59
	e_ψ	1.00	0.48	0.08	1.00	0.50	0.80	1.00	0.34	0.48

A. TRAJECTORY TRACKING

Under trajectory tracking, two categories will be discussed: pose tracking and thrust required to execute those tracking motions. The comparison metrics of RMSE, MAE and RSS related to trajectory tracking are reported in TABLE 10. Specifically, in this work, the MAE metric will facilitate the numerical comparison, and its bar charts are plotted as shown in FIGURE 11. For ease of comparison, the MAE ratio comparison is summarized in TABLE 11. As pose tracking is more crucial than twist tracking for the fish

TABLE 12. Trajectory Tracking — thrust ratio-comparison across CTC/IDC, Compensated-PID and Compensated-PD tested in simulated disturbances. Note: CTC/IDC is taken as the baseline for comparison in each disturbance scenario. The actual values are illustrated in FIGURE 17.

	S1: Disturbance ($0.0\,\mathrm{m/s}$)			S2: Disturbance ($0.5\,\mathrm{m/s}$)			S3: Disturbance ($0.9\,\mathrm{m/s}$)		
	CTC/IDC	Compensated-PID	Compensated-PD	CTC/IDC	Compensated-PID	Compensated-PD	CTC/IDC	Compensated-PID	Compensated-PD
f_{T_1}	1.00	0.94	0.46	1.00	1.36	1.03	1.00	1.13	1.08
f_{T_2}	1.00	0.98	0.51	1.00	1.53	1.17	1.00	1.43	1.13
f_{T_3}	1.00	1.01	0.55	1.00	1.30	0.91	1.00	1.12	0.93
f_{T_4}	1.00	1.07	0.59	1.00	1.45	1.13	1.00	1.36	0.95
f_{T_5}	1.00	1.22	0.48	1.00	1.17	1.19	1.00	1.68	1.47
f_{T_6}	1.00	1.33	0.51	1.00	1.54	1.15	1.00	1.95	1.58
f_{T_7}	1.00	1.12	0.46	1.00	1.19	0.88	1.00	1.44	1.20
f_{T_8}	1.00	1.45	0.54	1.00	1.43	1.14	1.00	1.64	1.14
mean	1.00	1.14	0.51	1.00	1.37	1.08	1.00	1.47	1.18

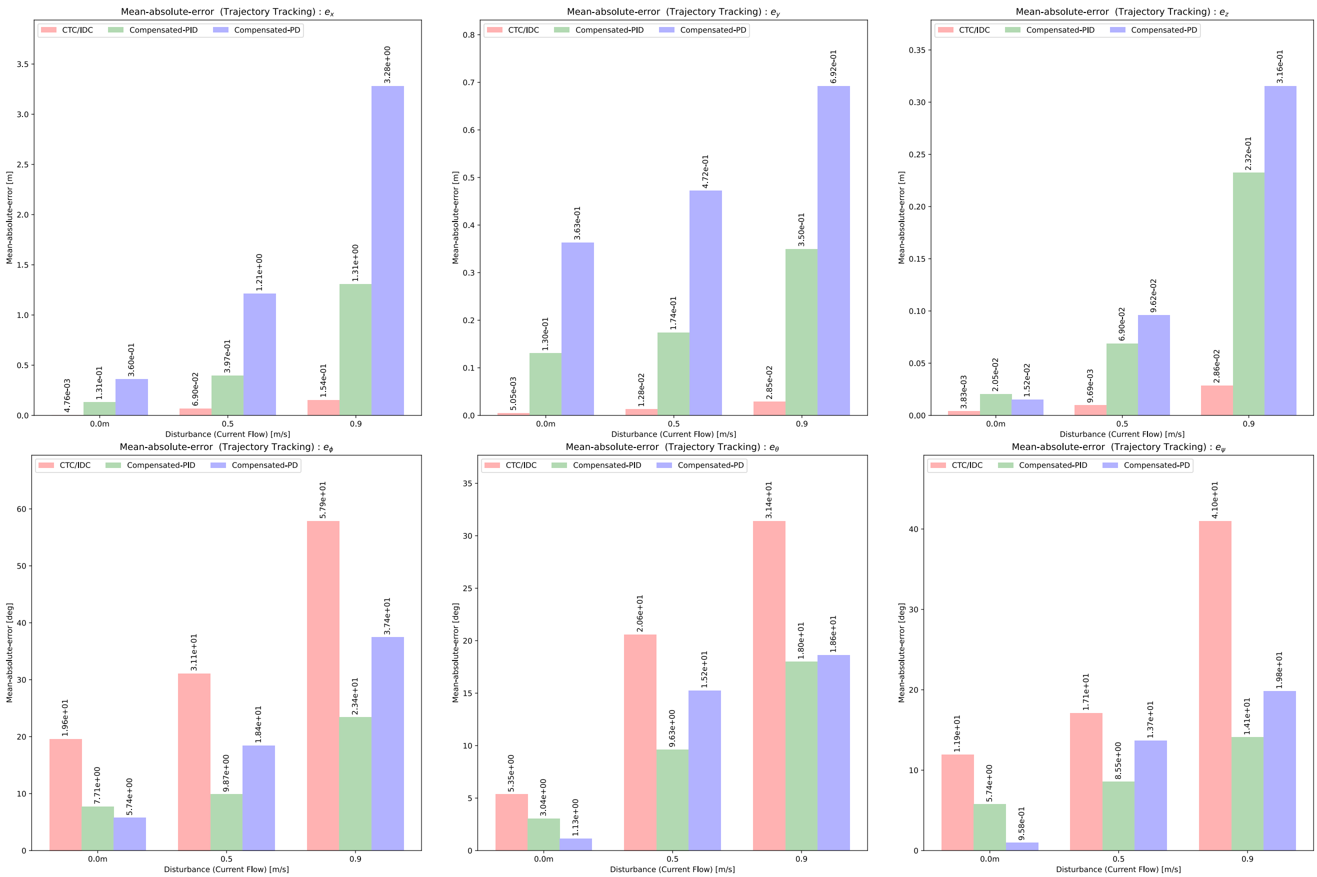

FIGURE 11. Trajectory Tracking — pose mean-absolute-error (MAE) of CTC/IDC, Compesnated-PID and Compensated-PD tested in simulated underwater-current disturbance($0.0\,\mathrm{m/s}$, $0.5\,\mathrm{m/s}$, $0.9\,\mathrm{m/s}$).

net-pen visual inspection, the discussion will only focus on pose tracking although all tracking results including twist tracking are reported in terms of RMSE, MAE and RSS as shown in TABLE 10 for the purpose of cross-validation by other researchers.

1) TRAJECTORY TRACKING — POSE TRACKING ERROR

As the UUV operates in a constrained operational environment, pose (position and orientation) tracking, especially position tracking, plays a crucial role in avoiding any damage to itself, the infrastructure, and the manpower involved. On the other hand, orientation tracking is essential to capture stable visual feedback for inspection purposes. FIGURE 12 shows, in three dimensions, the position tracking performance of CTC/IDC, Compensated-PID, and Compensated-PD in three types of simulated underwater current disturbances. In the graphical sense, it can be observed that CTC/IDC outperforms others in position tracking. From the proposed gain tuning methods, K_i gains in CTC/IDC and Compensated-PID contribute to relatively small steady-state error (except for e_z of Compensated-PID due to the relatively smaller K_i of e_z, compared to that of e_x and e_y) but result in higher oscillations whereas Compensated-PD has relatively fewer oscillations with large

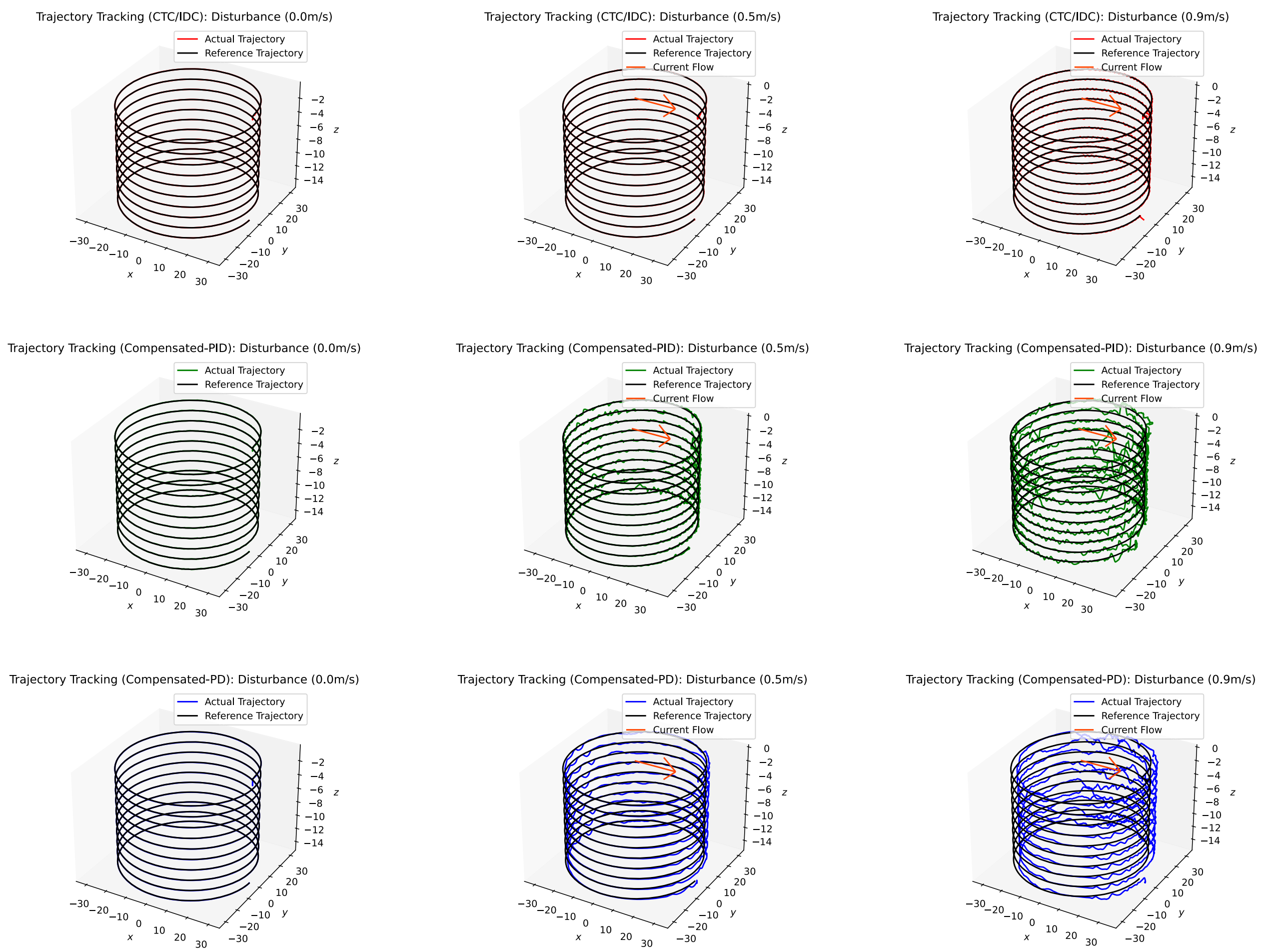

FIGURE 12. Trajectory tracking comparison among CTC/IDC, Compensated-PID and Compensated-PD tested in simulated underwater current disturbances. Disturbance: $0.0\,\mathrm{m/s}$ **(Left), Disturbance:** $0.5\,\mathrm{m/s}$ **(Middle), Disturbance:** $0.9\,\mathrm{m/s}$ **(Right).**

steady-state error. K_p and K_d gains of Compensated-PD and Compensated-PID are at least 2.5 times larger than those of CTC/IDC for position tracking. For the compensated controllers, K_d gains are slightly smaller than K_p gains, whereas for CTC/IDC, K_d gains are slightly larger than K_p. Having those large K_d gains seems to have the opposite effects instead of damping as mentioned in Remark 5.4. Under all underwater current disturbance scenarios, these behaviors can be observed consistently in FIGURE 13 and FIGURE 14. On the other hand, it is important to note that the sinusoidal-alike error plot in FIGURE 14 itself does not represent the oscillatory behaviors mentioned above but the high frequency on the sinusoidal-alike error indeed represents the oscillatory behaviors.

One common phenomenon across all controllers is that the position tracking performance deteriorates whenever the UUV faces directly toward the underwater current disturbance. This can be explained by Eqn. (13) which clearly shows horizontal thrusters' coupling in surge, sway and yaw motions — four thrusters generate the motions of 3-DoF at the same time and this behavior is previously highlighted in Remark 5.2. As the trajectory is designed such that the UUV faces tangential to the circumference of the fish net-pen, the controllers mainly generate sway motion while the external current disturbance attacks the surge direction of the UUV.

For the quantitative performance comparison, the numerical MAE ratio comparison as shown in TABLE 11 taking CTC/IDC as the baseline will be used. Under $0.5\,\mathrm{m/s}$ underwater current disturbance, the e_x of Compensated-PID and Compensated-PD are 5.75 and 17.6 times larger than that of CTC/IDC, respectively. The e_y of the compensated controllers are 13.7 and 37 times larger than that of CTC/IDC, respectively. In e_z, the error difference is smaller compared to e_x and e_y, and the compensated controllers yield 7.11 and 9.92 times larger errors than CTC/IDC, respectively. A similar pattern is observed under $0.9\,\mathrm{m/s}$ underwater current disturbance. In the physical sense for the worst-case scenario, the largest value of Compensated-PD's e_x is around $7\,\mathrm{m}$ and this frequent large error indicates that BlueROV2 Heavy Configuration has physical interactions

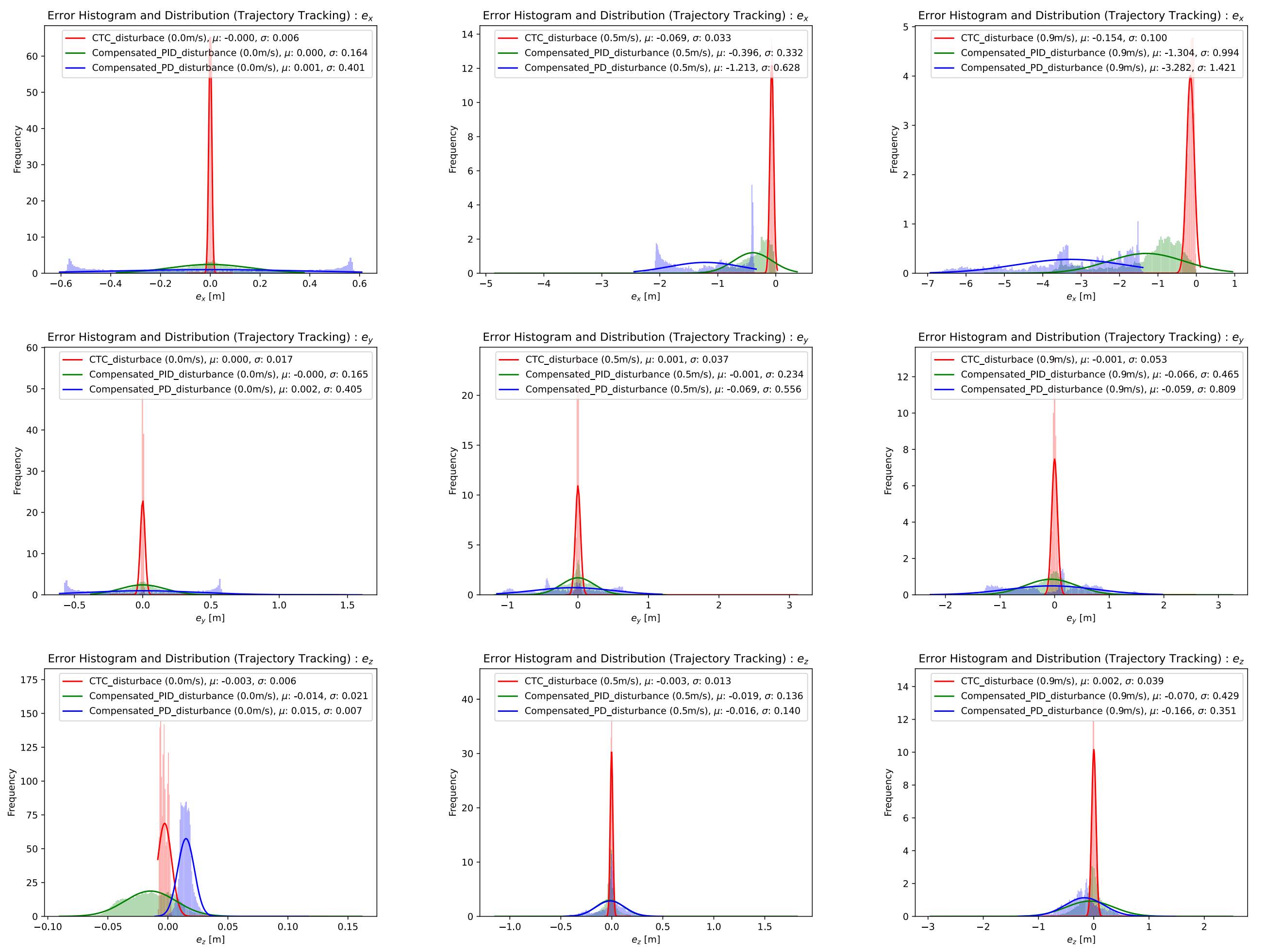

FIGURE 13. **Trajectory Tracking — position tracking error histogram and distribution. Disturbance:** 0.0 m/s **(Left), Disturbance:** 0.5 m/s **(Middle), Disturbance:** 0.9 m/s **(Right).**

with the infrastructure multiple times. For e_y, CTC/IDC's error is close to zero at all times except for the large error of around 3 m at the start. Both compensated controllers' errors are around 1.5 m to 2 m frequently. For e_z, the errors of compensated controllers vary around 1 m and the largest error of Compensated-PID can reach up to 3 m.

FIGURE 15 and 16 show the orientation tracking errors of the controllers under three underwater current disturbance scenarios. Although CTC/IDC outperforms compensated controllers in position tracking, its orientation tracking is inferior to the compensated controllers. The most interesting result is that under no underwater current disturbance, the orientation tracking performance of Compensated-PD is the best, but its performance deteriorates under underwater current disturbance. Therefore, the ideal scenario where the experiment is conducted without underwater current disturbance will convey absolutely misleading results. Under underwater current disturbances, Compensate-PID performs the best orientation tracking among all controllers.

K_p and K_d gains of all controllers for roll, pitch and yaw are larger than the linear counterparts except for z. However, the default values from the gain tuning methods for CTC/IDC result in large oscillations due to the relatively higher K_d gains as mentioned in Remark 5.4. Therefore, while keeping the default K_d gains, K_p and K_i gains of CTC/IDC for roll, pitch and yaw are increased. Although fine-tuning the gains for CTC/IDC results in better orientation tracking performance, its performance is still inferior to the compensated controller. Nonetheless, the orientation tracking error difference among controllers is not significant compared to the position tracking error. Under 0.5 m/s underwater current disturbance, the e_ϕ of Compensated-PID and Compensated-PD are 0.32 and 0.59 times smaller than that of CTC/IDC, respectively. The e_θ of the compensated controllers are 0.47 and 0.74 times smaller than that of CTC/IDC, respectively. Likewise, the e_ψ of the compensated controllers are 0.5 and 0.8 times smaller than that of CTC/IDC, respectively. A similar pattern is observed across all three controllers under 0.9 m/s underwater current disturbance. In the physical sense, all

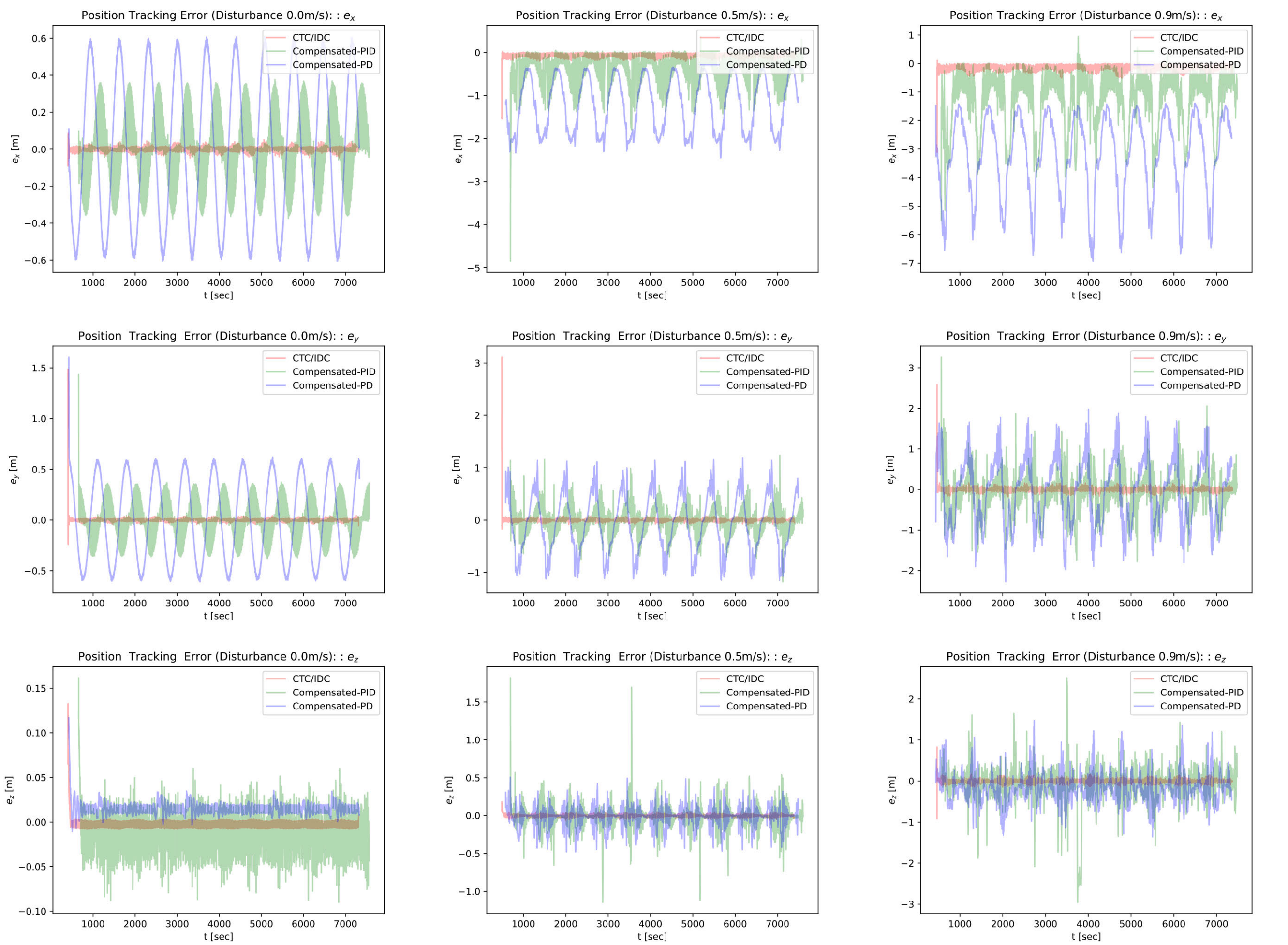

FIGURE 14. **Trajectory tracking — position tracking error comparison. Disturbance:** 0.0 m/s **(Left), Disturbance:** 0.5 m/s **(Middle), Disturbance:** 0.9 m/s **(Right).**

controllers' orientation errors in roll, pitch and yaw are as large as 175°, 80° and 175° respectively. Regardless, Compensated-PID's error varies around those values less frequently than others, achieving the best orientation tracking performance.

One possible way to explain holistically why CTC/IDC has a poor orientation tracking error is the use of model-based control with parametric uncertainty and unmodelled dynamics which are not canceled in CTC/IDC. Therefore, those uncanceled terms in the highly nonlinear and coupled moment equations (K, M, N) make control gain tuning for the orientation tracking more tedious than the position tracking.

Remark 7.1: The error distribution is not Gaussian in the statistical test using scipy.stats.normaltest which tests if the data set differs from a normal distribution [64]. However, in the graphical sense, most errors appear in the shape of a normal distribution. Therefore, mean and standard deviation of error distribution if necessary are reported for error comparison across controllers.

Remark 7.2: As the error distribution is not Gaussian, the root-mean-square-error (RMSE) metric alone may not be sufficient for error comparison [65]. In addition, RMSE is prone to outliers. Therefore, in addition to RMSE, mean-absolute-error (MAE) and root-sum-squared (RSS) metrics are reported for error comparison across controllers.

Remark 7.3: The histogram is normalized such that the area under the histogram is 1.

Remark 7.4: This study simulates, validates, and compares the performances of Compensated-PD, Compensated-PID, and CTC/IDC. As presented in Section I, these controllers are selected for their cost-effectiveness, practicality, and widespread applications in academic and industrial settings [27], [35]. While acknowledging the existence of more advanced controllers suitable for application, simulation, and validation using the proposed simulation platform, the scope of this paper, along with its length constraints, limits the in-depth exploration of these advanced controllers. Indeed, this paper discusses a holistic analysis and synthesis of a standard offshore aquaculture fish net-pen visual

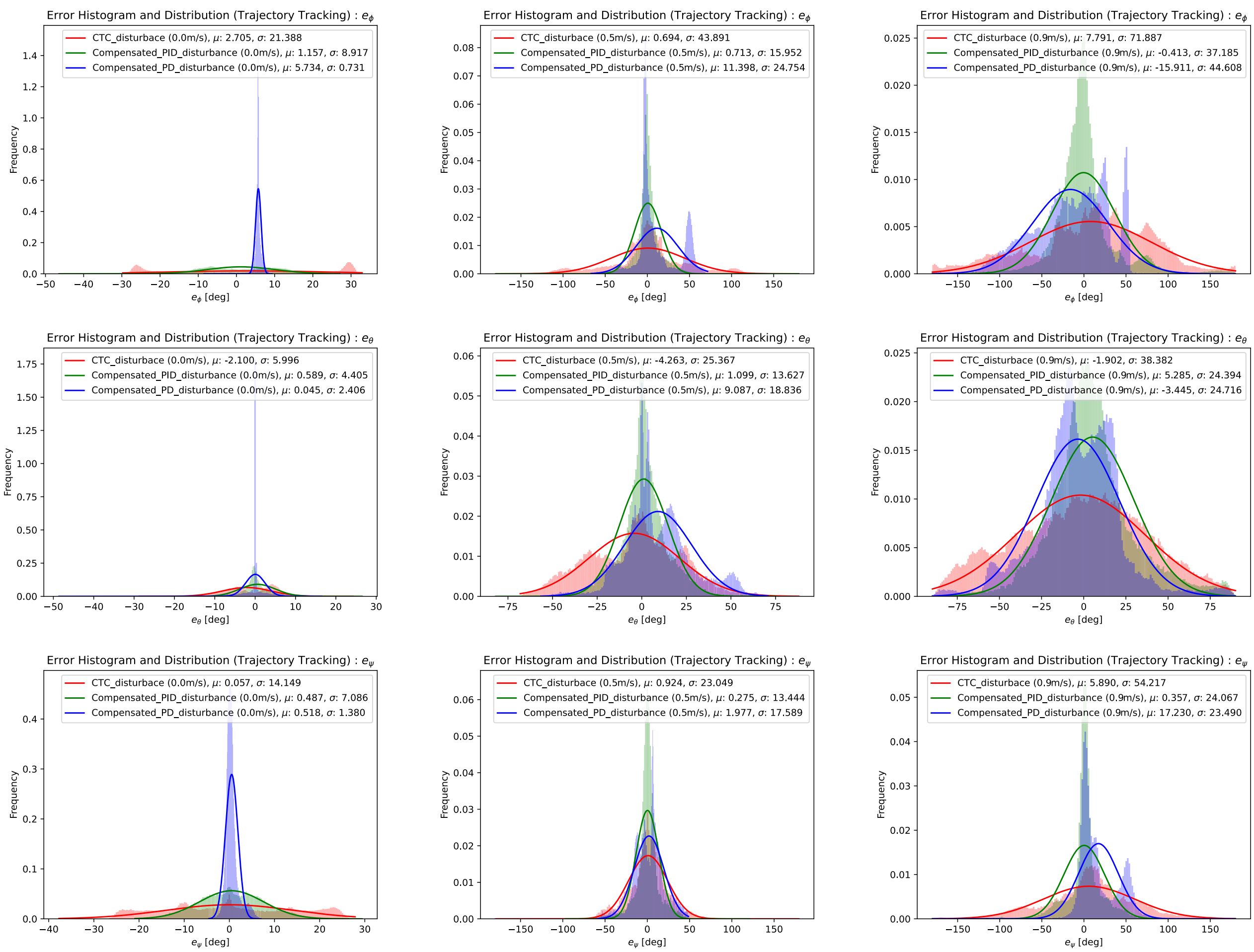

FIGURE 15. Trajectory tracking — orientation tracking error histogram and distribution. Disturbance: $0.0\,\mathrm{m/s}$ **(Left), Disturbance:** $0.5\,\mathrm{m/s}$ **(Middle), Disturbance:** $0.9\,\mathrm{m/s}$ **(Right).**

inspection using high-fidelity simulation. A separate paper will be dedicated to addressing more advanced controllers. Meanwhile, ongoing efforts involve the development and experimental testing of more advanced controllers.

2) TRAJECTORY TRACKING — THRUST

After the analysis of pose tracking performance, it is appropriate to evaluate the required/generated thrust to execute the pose tracking motions. This is to cross-validate if the better controller performance is achieved at the cost of excessive thrust requirement — high power consumption. For thrust analysis, FIGURE 17 shows each T200 thruster's total thrust for the controller under different underwater current disturbances. Using those total thrust values, thrust ratio comparison is generated for ease of comparison as shown in TABLE 12. FIGURE 18 shows each T200 thruster's thrust histogram from which the maximum rated thrust constraint of 31.25 N according to Eqn (44) can be observed.

Under the underwater current disturbances, the total thrust of each T200 thruster for CTC/IDC is generally smaller than that of compensated controllers. To generalize this statement by utilizing the benefit of the same unit (N), the mean total thrust value for each controller under different underwater current disturbances is calculated as shown in TABLE 12. Under $0.5\,\mathrm{m/s}$ underwater current disturbance, Compensated-PID and Compensated-PD require 37 % and 8 % more thrust than CTC/IDC, respectively. Similarly, under $0.9\,\mathrm{m/s}$ underwater current disturbance, Compensated-PID and Compensated-PD require 47 % and 18 % more thrust than CTC/IDC.

Remark 7.5: As the relationship between thrust and power is nonlinear, the analysis in this work will be targeted to thrust directly. The exploration on power and Energy consumption of controllers will be future work.

Remark 7.6: As a T200 thruster generates both forward (+) and reverse (−) thrust, the total thrust is calculated by summing the absolute thrust value.

B. OVERALL PERFORMANCE

In terms of overall trajectory tracking, CTC/IDC offers the best performance utilizing the minimum thrust under $0.5\,\mathrm{m/s}$ and $0.9\,\mathrm{m/s}$ underwater current disturbances. For the pose

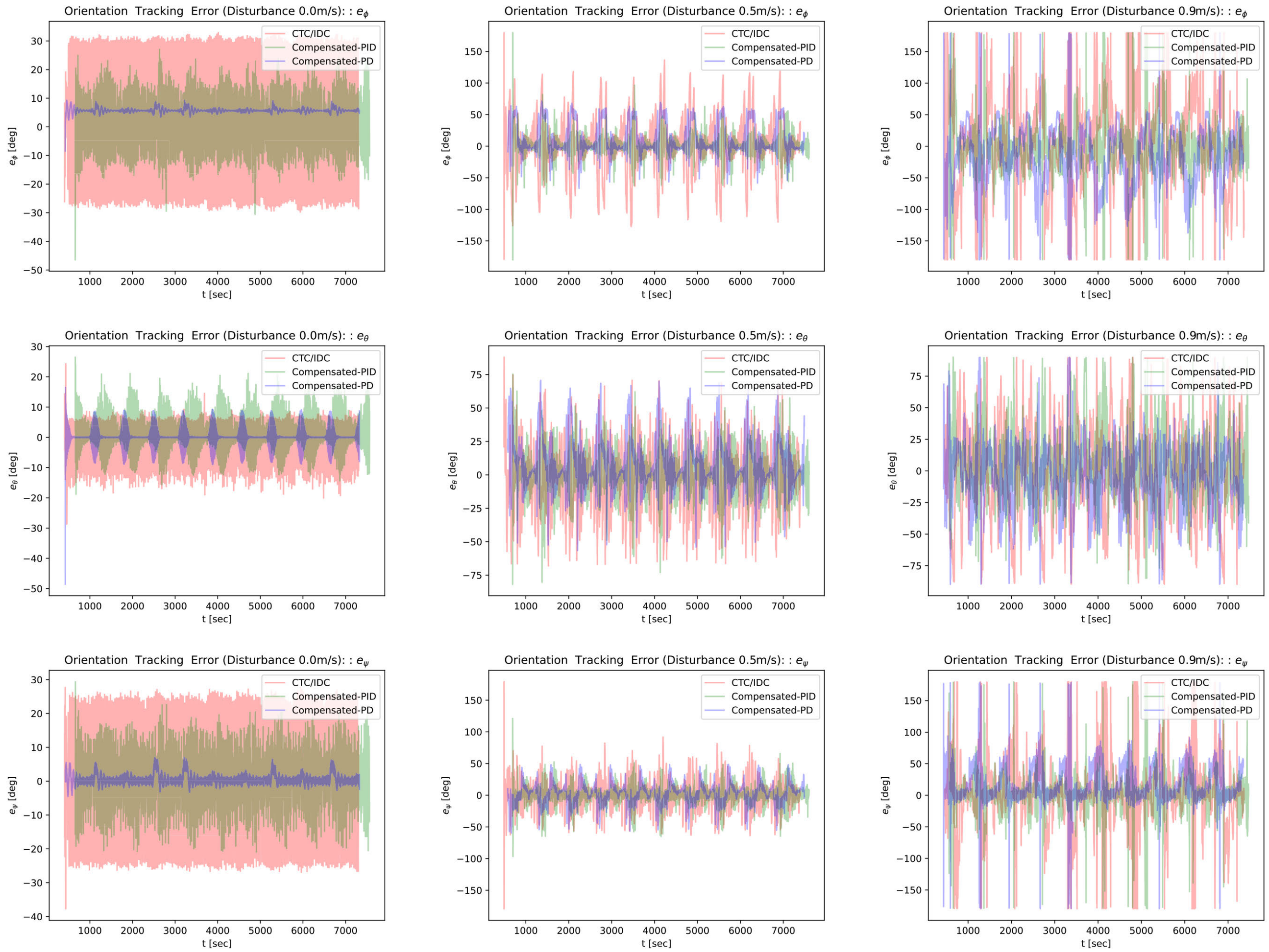

FIGURE 16. **Trajectory tracking — orientation tracking error comparison. Disturbance:** 0.0 m/s **(Left), Disturbance:** 0.5 m/s **(Middle), Disturbance:** 0.9 m/s **(Right).**

tracking, the errors of Compensated-PID and Compensated-PD are 5.75 - 24.3 times larger than CTC/IDC, whereas their orientation tracking errors are 0.32 - 0.8 times smaller than CTC/IDC. In the physical sense, Compensated-PID and Compensated-PD's e_x can reach up to 5 m and 7 m respectively. This frequent large e_x indicates that BlueROV2 Heavy Configuration has physical interactions with the infrastructure multiple times, noting that the designated gap between the UUV and fish net-pen is 4 m and the gap between the sinker tube cable and the UUV is approximately about 2 m. On the other hand, the orientation tracking error of all controllers can reach up to 175° and Compensated-PID has the least frequency to have that error value. In addition, Compensated-PID and Compensated-PD require 37-47 % and 8-18 % more thrust than CTC/IDC, respectively. Therefore, CTC/IDC outperforms Compensated-PID and Compensated-PD and, to a greater extent, with the improvement in the orientation tracking if achieved.

For fish net-pen visual inspection in a constrained environment, controllers' performance on minimum trajectory tracking error is desired to avoid damage to the fish net-pen and itself. In fact, pose tracking plays a relatively more crucial role than twist tracking. For the visual inspection, a stable visual feedback from a desired pose is essential, whereas the motion along a desired twist is preferable. To fulfill this objective, CTC/IDC has the potential to perform significantly better due to the model-based approach for the field trial with environmental disturbance. On the other hand, Compensated-PID and Compensated-PD could potentially result in physical interaction with the infrastructure according to the simulation results under 0.5 m/s and 0.9 m/s underwater current disturbances.

C. ADVANTAGES AND DRAWBACKS OF CTC/IDC

As CTC/IDC is a model-based control, advantages and drawbacks result from the dynamic model. That is the reason why a dedicated section on dynamic modelling, Section: III is detailed with theoretical and practical concerns.

As the advantages, four points will be discussed: well-predicted/bounded controller output, the resulting minimum

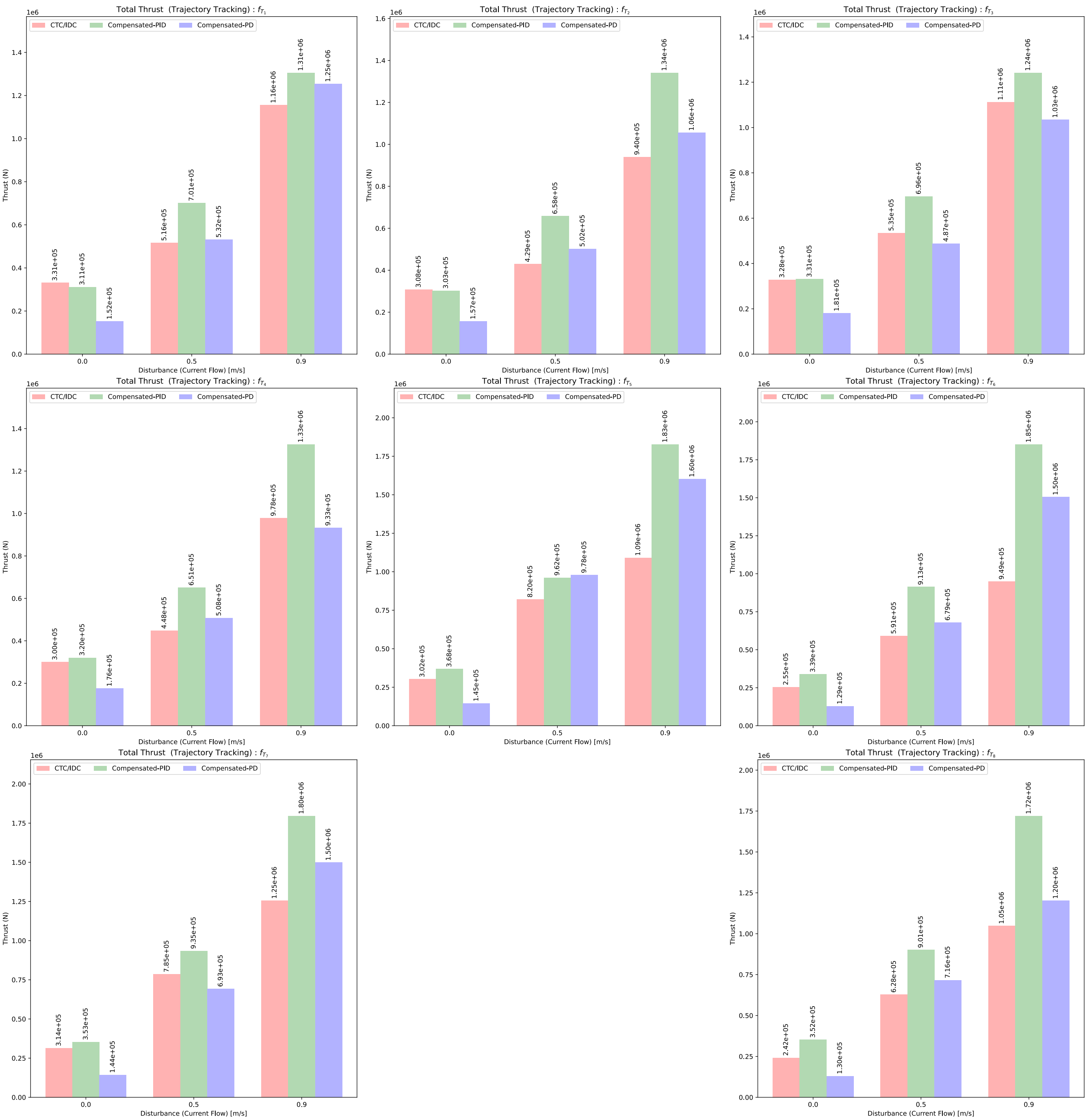

FIGURE 17. **Trajectory tracking — thrust comparison of CTC/IDC, Compesnated-PID and Compensated-PD tested in simulated underwater-current disturbance(**$0.0\,\mathrm{m/s}$**,** $0.5\,\mathrm{m/s}$**,** $0.9\,\mathrm{m/s}$**).**

thrust output, disturbance rejection and degree of freedom in the balance between PID and dynamic model. Firstly, as the nonlinear terms are updated at run-time and PID gains are chosen by the control designers, the controller output is well-predicted/bounded as long as PID gains are not dominant over nonlinear terms. Secondly, CTC/IDC generates only the required control authority governed by the dynamic model, and thus, the generated thrust is minimal compared to model-free control. Thirdly, the effects (e.g., additional velocity) of disturbance (e.g., underwater current) on the system are reflected in the nonlinear terms, which are the canceling terms and the resulting errors are also reflected in PID part of CTC/IDC. By those means, CTC/IDC can handle disturbance rejection well compared to model-free control. Finally, CTC/IDC offers the control designer the freedom to set the balance between PID and dynamic model.

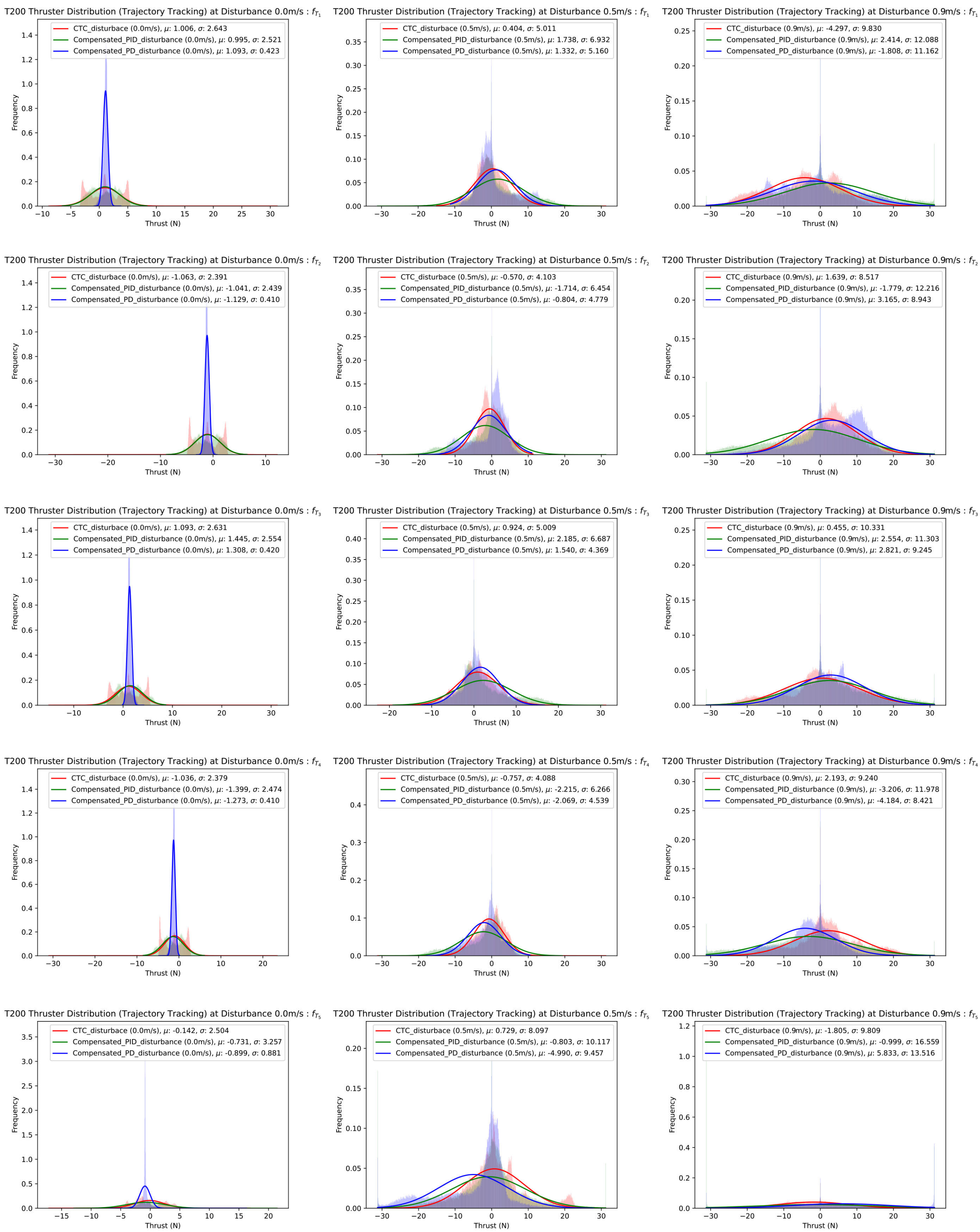

FIGURE 18. **Trajectory Tracking – thrust histogram and distribution of CTC/IDC, Compesnated-PID and Compensated-PD tested in simulated underwater-current disturbance(**$0.0\,\mathrm{m/s}$**,** $0.5\,\mathrm{m/s}$**,** $0.9\,\mathrm{m/s}$**).**

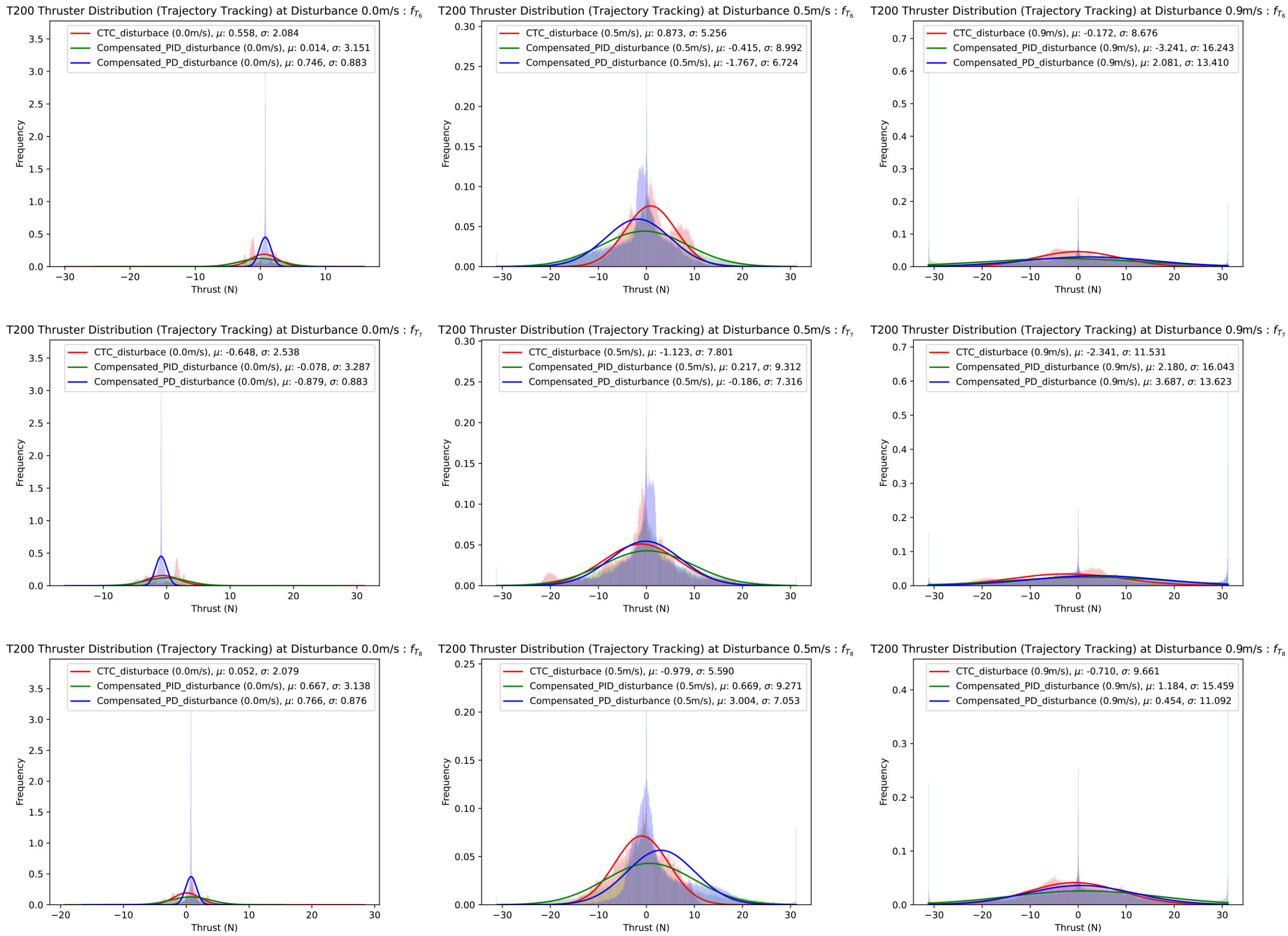

FIGURE 18. ***(Continued.)*** **Trajectory Tracking — thrust histogram and distribution of CTC/IDC, Compesnated-PID and Compensated-PD tested in simulated underwater-current disturbance(**$0.0\,\mathrm{m/s}$**,** $0.5\,\mathrm{m/s}$**,** $0.9\,\mathrm{m/s}$**).**

Certainly, setting all high PID gains defeats the purpose. Thus, one possible scenario is setting high PID gains only over highly nonlinear and coupled parts of the dynamic model and keeping the nature of the remaining nonlinear terms.

On the other hand, CTC/IDC attracts drawbacks due to its dynamic model, namely parametric uncertainty and unmodelled dynamics. Firstly, parametric uncertainty is a crucial matter, and as mentioned in the dynamic modeling section, most of the nonlinear coefficients are approximated by the empirical study in Gazebo or referred from the existing literature, which suggests different values among different literature. Secondly, there are certainly unmodelled dynamics in the model-based approach, as the first principle equations cannot describe all dynamics exhibited in nature. For instance, only up to quadratic damping coefficients are utilized in this work, and higher terms are neglected.

Therefore, there needs to be a proper experimental study to determine the suitability of CTC/IDC. The more system parameters are available and reflected in the dynamic model, the better CTC/IDC's performance can be formulated and designed.

VIII. CONCLUSION

In this paper, high-fidelity experimental simulation studies of UUV such as BlueROV2 Heavy Configuration to be deployed in fish net-pen visual inspection in offshore aquaculture were conducted under $0.0\,\mathrm{m/s}$, $0.5\,\mathrm{m/s}$ and $0.9\,\mathrm{m/s}$ underwater current disturbances. A standard task scenario of an offshore aquaculture fish net-pen visual inspection was discussed in detail, and three controllers, namely Compensated-PD, Compensated-PID and CTC/IDC schemes, were implemented on 6 DoF BlueROV2 Heavy Configuration to track a 4 DoF helical trajectory. The task scenario was formulated based on the Blue Endeavour project of the New Zealand King Salmon Company located 5 kilometers due north of Cape Lambert, in northern Marlborough in consideration of many available and physically quantifiable parameters of the fish farm and BlueROV2 Heavy Configuration. While utilizing the minimum thrust, CTC/IDC outperforms

Compensated-PID and Compensated-PD in overall trajectory tracking under different underwater current disturbances. Future works will cover more advanced controllers focusing on the energy-optimal control schemes, related stability and robustness analysis on linear and nonlinear UUV models.

ACKNOWLEDGMENT

The authors acknowledge the financial support of the Blue Economy Cooperative Research Centre (CRC), Australia. The authors thank the graduate research facilities provided by the Auckland University of Technology. They also thank Phone Thiha Kyaw and Sai Htet Moe Swe for their initial technical support in ROS setup and troubleshooting.

REFERENCES

[1] M. C. Beveridge, "Cage and pen fish farming: Carrying capacity models and environmental impact," Food & Agricult. Org. Fisheries, Rome, Italy, Tech. Rep., 255, 1984.

[2] D. Cressey, "Review of cage and containment tank designs for offshore fish farming," *Nature*, vol. 458, pp. 398–400, Jan. 2009

[3] Y. I. Chu, C. M. Wang, J. C. Park, and P. F. Lader, "Review of cage and containment tank designs for offshore fish farming," *Aquaculture*, vol. 519, Mar. 2020, Art. no. 734928.

[4] I. López Mengual, P. Sanchez-Jerez, and J. Ballester-Berman, "Offshore aquaculture as climate change adaptation in coastal areas: Sea surface temperature trends in the western Mediterranean Sea," *Aquaculture Environ. Interact.*, vol. 13, pp. 515–526, Dec. 2021.

[5] T. McClure. *Major New Zealand Salmon Producer Shuts Farms as Warming Waters Cause Mass Die-Offs*. Accessed: Nov. 3, 2022. [Online]. Available: https://www.theguardian.com/world/2022/may/26/major-new-zealand-salmon-producer-shuts-farms-as-warming-waters-cause-mass-die-offs

[6] I. Fitridge, T. Dempster, J. Guenther, and R. de Nys, "The impact and control of biofouling in marine aquaculture: A review," *Biofouling*, vol. 28, no. 7, pp. 649–669, Aug. 2012.

[7] S. J. Ohrem, E. Kelasidi, and N. Bloecher, "Analysis of a novel autonomous underwater robot for biofouling prevention and inspection in fish farms," in *Proc. 28th Medit. Conf. Control Autom. (MED)*, Sep. 2020, pp. 1002–1008.

[8] H. B. Amundsen, W. Caharija, and K. Y. Pettersen, "Autonomous ROV inspections of aquaculture net pens using DVL," *IEEE J. Ocean. Eng.*, vol. 47, no. 1, pp. 1–19, Jan. 2022.

[9] F. K. Myrhol. *Most Fish Escape Due to Holes in the Net*. Accessed: Nov. 8, 2022. [Online]. Available: https://forskning.no/fiskeri–og-havbruksnaeringens-forskningsfond-fiskerifag-oppdrett/flest-fisk-rommer-pa-grunn-av-hull-i-not/1595515

[10] D. Jackson, A. Drumm, S. McEvoy, Ø. Jensen, D. Mendiola, G. Gabiña, J. A. Borg, N. Papageorgiou, Y. Karakassis, and K. D. Black, "A pan-European valuation of the extent, causes and cost of escape events from sea cage fish farming," *Aquaculture*, vol. 436, pp. 21–26, Jan. 2015.

[11] W. Liao, S. Zhang, Y. Wu, D. An, and Y. Wei, "Research on intelligent damage detection of far-sea cage based on machine vision and deep learning," *Aquacultural Eng.*, vol. 96, Feb. 2022, Art. no. 102219.

[12] C. Wang, Z. Li, T. Wang, X. Xu, X. Zhang, and D. Li, "Intelligent fish farm—The future of aquaculture," *Aquaculture Int.*, vol. 29, no. 6, pp. 2681–2711, Dec. 2021.

[13] W. Akram, A. Casavola, N. Kapetanović, and N. Miškovic, "A visual servoing scheme for autonomous aquaculture net pens inspection using ROV," *Sensors*, vol. 22, no. 9, p. 3525, May 2022.

[14] H. Ø. Karlsen, H. B. Amundsen, W. Caharija, and M. Ludvigsen, "Autonomous aquaculture: Implementation of an autonomous mission control system for unmanned underwater vehicle operations," in *Proc. Oceans*, Sep. 2021, pp. 1–10.

[15] C. C. Constantinou, G. P. Georgiades, and S. G. Loizou, "A laser vision system for relative 3-D posture estimation of an underwater vehicle with hemispherical optics," *Robotics*, vol. 10, no. 4, p. 126, Nov. 2021.

[16] M. Bjerkeng, T. Kirkhus, W. Caharija, J. T. Thielemann, H. B. Amundsen, S. Johan Ohrem, and E. Ingar Grøtli, "ROV navigation in a fish cage with laser-camera triangulation," *J. Mar. Sci. Eng.*, vol. 9, no. 1, p. 79, Jan. 2021.

[17] D. A. Duecker, T. Hansen, and E. Kreuzer, "RGB-D camera-based navigation for autonomous underwater inspection using low-cost micro AUVs," in *Proc. IEEE/OES Auto. Underwater Vehicles Symp. (AUV)*, Sep. 2020, pp. 1–7.

[18] S. Paspalakis, K. Moirogiorgou, N. Papandroulakis, G. Giakos, and M. Zervakis, "Automated fish cage net inspection using image processing techniques," *IET Image Process.*, vol. 14, no. 10, pp. 2028–2034, Aug. 2020.

[19] Q. Tao, K. Huang, C. Qin, B. Guo, R. Lam, and F. Zhang, "Omnidirectional surface vehicle for fish cage inspection," in *Proc. Oceans*, Oct. 2018, pp. 1–6.

[20] H. Lee, D. Jeong, H. Yu, and J. Ryu, "Autonomous underwater vehicle control for fishnet inspection in turbid water environments," *Int. J. Control, Autom. Syst.*, vol. 20, no. 10, pp. 3383–3392, Oct. 2022.

[21] N. Kapetanovic, D. Nad, and N. Mišković, "Towards a heterogeneous robotic system for autonomous inspection in mariculture," in *Proc. Oceans*, Sep. 2021, pp. 1–6.

[22] W. Zhang, P. Han, Y. Liu, Y. Zhang, W. Wu, and Q. Wang, "Design of an improved adaptive slide controller in UUV dynamic base recovery," *Ocean Eng.*, vol. 285, Oct. 2023, Art. no. 115266.

[23] X. Shang, Y. Zhao, Z. Wang, Y. He, E. Zhao, and X. Deng, "Finite-time tracking for UUV with system uncertainty using fast adaptive nonsingular terminal high-order sliding mode control," in *Proc. Oceans*, Jun. 2023, pp. 1–6.

[24] J. Li, Y. Xia, G. Xu, Z. He, K. Xu, and G. Xu, "Three-dimensional prescribed performance tracking control of UUV via PMPC and RBFNN-FTTSMC," *J. Mar. Sci. Eng.*, vol. 11, no. 7, p. 1357, Jul. 2023.

[25] W. Gan, T. Xia, and Z. Chu, "A prognosis technique based on improved GWO-NMPC to improve the trajectory tracking control system reliability of unmanned underwater vehicles," *Electronics*, vol. 12, no. 4, p. 921, Feb. 2023.

[26] X. Wang, B. Xu, and Y. Guo, "Fuzzy logic system-based robust adaptive control of AUV with target tracking," *Int. J. Fuzzy Syst.*, vol. 25, no. 1, pp. 338–346, Feb. 2023.

[27] K. J. Åström and T. Hägglund, "The future of PID control," *Control Eng. Pract.*, vol. 9, no. 11, pp. 1163–1175, Nov. 2001.

[28] H. Cho, S.-K. Jeong, D.-H. Ji, N.-H. Tran, M. T. Vu, and H.-S. Choi, "Study on control system of integrated unmanned surface vehicle and underwater vehicle," *Sensors*, vol. 20, no. 9, p. 2633, May 2020.

[29] Z. Guangyi, Z. Qingjun, Z. Zhiyu, D. Xiaoqiang, Z. Chunlei, and D. Xiaoqiang, "Research on underwater safety inspection and operational robot motion control," in *Proc. 33rd Youth Academic Annu. Conf. Chin. Assoc. Autom. (YAC)*, May 2018, pp. 322–327.

[30] S. Soylu, A. A. Proctor, R. P. Podhorodeski, C. Bradley, and B. J. Buckham, "Precise trajectory control for an inspection class ROV," *Ocean Eng.*, vol. 111, pp. 508–523, Jan. 2016.

[31] Y. Zhang, J. Che, Y. Hu, J. Cui, and J. Cui, "Real-time ocean current compensation for AUV trajectory tracking control using a meta-learning and self-adaptation hybrid approach," *Sensors*, vol. 23, no. 14, p. 6417, Jul. 2023.

[32] Y. Sola, G. Le Chenadec, and B. Clement, "Simultaneous control and guidance of an AUV based on soft Actor–Critic," *Sensors*, vol. 22, no. 16, p. 6072, Aug. 2022.

[33] R. Hernández-Alvarado, L. García-Valdovinos, T. Salgado-Jiménez, A. Gómez-Espinosa, and F. Fonseca-Navarro, "Neural network-based self-tuning PID control for underwater vehicles," *Sensors*, vol. 16, no. 9, p. 1429, Sep. 2016.

[34] O. A. Aguirre-Castro, E. Inzunza-González, E. E. García-Guerrero, E. Tlelo-Cuautle, O. R. López-Bonilla, J. E. Olguín-Tiznado, and J. R. Cárdenas-Valdez, "Design and construction of an ROV for underwater exploration," *Sensors*, vol. 19, no. 24, p. 5387, Dec. 2019.

[35] Z. Bingul and K. Gul, "Intelligent-PID with PD feedforward trajectory tracking control of an autonomous underwater vehicle," *Machines*, vol. 11, no. 2, p. 300, Feb. 2023.

[36] T. T. Tun and L. Huang, "Working environments and controller design for unmanned underwater vehicles in offshore aquaculture—A review," Presented at the 22nd Int. Conf. Control, Automat. Syst. (ICCAS), Busan, South Korea, Nov. 2022.

[37] *BlueROV2 Heavy Configuration Retrofit Kit*. Accessed: Aug. 2, 2023. [Online]. Available: https://bluerobotics.com/store/rov/bluerov2-upgrade-kits/brov2-heavy-retrofit/

[38] S. Pedersen, J. Liniger, F. F. Sørensen, K. Schmidt, M. V. Benzon, and S. S. Klemmensen, "Stabilization of a ROV in three-dimensional space using an underwater acoustic positioning system," *IFAC-PapersOnLine*, vol. 52, no. 17, pp. 117–122, 2019.

[39] Y. Cao, B. Li, Q. Li, A. A. Stokes, D. M. Ingram, and A. Kiprakis, "A nonlinear model predictive controller for remotely operated underwater vehicles with disturbance rejection," *IEEE Access*, vol. 8, pp. 158622–158634, 2020.

[40] Q. Li, Y. Cao, B. Li, D. M. Ingram, and A. Kiprakis, "Numerical modelling and experimental testing of the hydrodynamic characteristics for an open-frame remotely operated vehicle," *J. Mar. Sci. Eng.*, vol. 8, no. 9, p. 688, Sep. 2020.

[41] S. Rúa and R. E. Vásquez, "Development of a low-level control system for the ROV Visor3," *Int. J. Navigat. Observ.*, vol. 2016, pp. 1–12, Jul. 2016.

[42] J. González-García, N. A. Narcizo-Nuci, L. G. García-Valdovinos, T. Salgado-Jiménez, A. Gómez-Espinosa, E. Cuan-Urquizo, and J. A. E. Cabello, "Model-free high order sliding mode control with finite-time tracking for unmanned underwater vehicles," *Appl. Sci.*, vol. 11, no. 4, p. 1836, Feb. 2021.

[43] *Uuv_Simulator: Unmanned Underwater Vehicle (UUV) Simulation With Gazebo*. Accessed: Jan. 19, 2023. [Online]. Available: https://github.com/uuvsimulator/uuv_simulator

[44] M. M. M. Manhães, S. A. Scherer, M. Voss, L. R. Douat, and T. Rauschenbach, "UUV simulator: A gazebo-based package for underwater intervention and multi-robot simulation," in *Proc. Oceans*, Sep. 2016, pp. 1–8.

[45] *BlueROV2*. Accessed: Nov. 2, 2022. [Online]. Available: https://bluerobotics.com/store/rov/bluerov2/

[46] *Gazebo*. Accessed: Dec. 15, 2022. [Online]. Available: https://gazebosim.org/home.

[47] T. I. Fossen, *Handbook of Marine Craft Hydrodynamics and Motion Control*. Hoboken, NJ, USA: Wiley, 2011.

[48] G. Antonelli, *Underwater Robots*. Cham, Switzerland: Springer, 2018.

[49] *Unmanned Underwater Vehicle Simulator Documentation: Actuators*. Accessed: Jan. 19, 2023. [Online]. Available: https://uuvsimulator.github.io/packages/uuv/_simulator/docs/features/actuators/

[50] D. R. Yoerger, J. G. Cooke, and J.-J.-E. Slotine, "The influence of thruster dynamics on underwater vehicle behavior and their incorporation into control system design," *IEEE J. Ocean. Eng.*, vol. 15, no. 3, pp. 167–178, Jul. 1990.

[51] *T200 Thruster: Under Technical Details*. Accessed: Jan. 19, 2023. [Online]. Available: https://bluerobotics.com/store/thrusters/t100-t200-thrusters/t200-thruster-r2-rp/

[52] *MATLAB and Simulink Robotics Arena: From Data to Model*. Accessed: Jan. 26, 2023. [Online]. Available: https://au.mathworks.com/matlabcentral/fileexchange/65919-MATLAB-and-simulink-robotics-arena-from-data-to-model

[53] C.-J. Wu, "6-DoF modelling and control of a remotely operated vehicle," M.S. thesis, College Sci. Eng., Flinders Univ., Adelaide, SA, Australia, 2018.

[54] M. D. Council, *Decision of Marlborough District Council*, document RAD0141-U180796, 2022, pp. 1–201.

[55] E. Newcombe, B. Knight, M. Smeaton, H. Bennett, L. Mackenzie, M. Scheel, R. Vennell, and C. Campos, "Water column assessment for a proposed salmon farm offshore of the Marlborough sounds," Prepared The New Zealand King Salmon Co. Ltd., Cawthron, Nelson, New Zealand, Tech. Rep., 3313, p. 96, 2020.

[56] *Blue Endeavour: Our Open Ocean Farm Proposl*. Accessed: Nov. 16, 2022. [Online]. Available: https://www.kingsalmon.co.nz/open-ocean-blue-endeavour/

[57] K. M. Lynch and F. C. Park, *Modern Robotics*. Cambridge, U.K.: Cambridge Univ. Press, 2017.

[58] K. Ogata, *Modern Control Engineering*. Upper Saddle River, NJ, USA: Prentice-Hall, 2010.

[59] K. J. Åström and T. Hägglund, *PID Controllers: Theory, Design and Tuning*, 2nd ed. Triangle Park, NC, USA: Instrum. Soc. Amer., Res. 1995.

[60] *RQT_TF_Tree*. Accessed: Oct. 5, 2023. [Online]. Available: http://wiki.ros org/rqt_tf_tree

[61] *RVIZ*. Accessed: Oct. 5, 2023. [Online]. Available: http://wiki.ros.org/rviz

[62] *Blender*. Accessed: Dec. 15, 2022. [Online]. Available: https://www.blender.org/

[63] J.-K. Choi, T. Shiraishi, and T. Tanaka, "Safe breakwater-following control of an autonomous underwater vehicle with non-zero forward velocity," *Autom. Construct.*, vol. 16, no. 6, pp. 778–786, Sep. 2007.

[64] *Scipy. Stats. Normaltest*. Accessed: Oct. 5, 2023. [Online]. Available: https://docs.scipy.org/doc/scipy/reference/generated/scipy.stats.normaltest.html

[65] T. O. Hodson, "Root-mean-square error (RMSE) or mean absolute error (MAE): When to use them or not," *Geosci. Model Develop.*, vol. 15, no. 14, pp. 5481–5487, Jul. 2022.

THEIN THAN TUN (Graduate Student Member, IEEE) received the Diploma degree in mechatronic engineering from Ngee Ann Polytechnic, Singapore, in 2012, and the B.E. degree in engineering product development (EPD) from SUTD, in 2016. He is currently pursuing the Ph.D. degree with the Auckland University of Technology (AUT), New Zealand. Before joining AUT, he worked in the robotics industry and academic research laboratory with the Singapore University of Technology and Design (SUTD).

LOULIN HUANG (Member, IEEE) received the bachelor's and master's degrees in mechanical engineering from the Huazhong University of Science and Technology, China, the master's degree in electrical and electronic engineering from Nanyang Technology University, Singapore, and the Ph.D. degree from the National University of Singapore. He has about 35 years' experience in the research and teaching in the areas of mechatronics and robotics with a distinctively interdisciplinary flavor. He is currently an Associate Professor of mechatronics with the Department of Mechanical Engineering, Auckland University of Technology. He has completed more than 30 industrial and government-funded projects in a wide range of industrial applications. He has (co)authored more than 140 research publications.

MARK ANTHONY PREECE received the master's degree in marine science from the University of Otago, Aotearoa, New Zealand, and the Postgraduate Diploma degree in business studies from Massey University, Aotearoa. He is currently the Seawater Manager with New Zealand King Salmon Company. He has around 30 years' of practical experience in the aquaculture industry, mainly focused on salmonids. The experience has involved managing and running salmon farming operations, undertaking research on nutritional aspects of farmed salmon and abalone, as well as applications and managing the practical design process for open ocean aquaculture farms. He has (co)authored more than 15 research publications.